Chem

CellPress

Observation of a Potential-Dependent Switch of Water Oxidation Mechanism on Co-Oxide-Based Catalysts

Chaochao Lang[1,3], Jingyi Li[1,3], Ke R. Yang[2,3], Yuanxing Wang[1,3], Da He[1], James E. Thorne[1], Seth Croslow[1], Qi Dong[1], Yanyan Zhao[1], Gabriela Prostko[1], Gary W. Brudvig[2], Victor S. Batista[2*], Matthias M. Waegele[1**], Dunwei Wang[1,4***]

[1]Department of Chemistry, Merkert Chemistry Center, Boston College, 2609 Beacon St., Chestnut Hill, Massachusetts， 02467, United States

[2]Yale Energy Sciences Institute and Department of Chemistry, Yale University, New Haven, Connecticut 06520, United States

[3]These authors contributed equally.

[4]Lead Contact

*Correspondence: victor.batista@yale.edu

**Correspondence: waegele@bc.edu

***Correspondence: dunwei.wang@bc.edu

SUMMARY

O-O bond formation is a key elementary step of the water oxidation reaction. However, it is still unclear how the mechanism of O-O coupling depends on the applied electrode potential. Herein, using water-in-salt electrolytes, we systematically altered the water activity, which enabled us to probe the O-O bond forming mechanism on heterogeneous Co-based catalysts as a function of applied potential. We discovered that the water oxidation mechanism is sensitive to the applied potential: At relatively low driving force, the reaction proceeds through an intramolecular oxygen coupling mechanism, whereas the water nucleophilic attack mechanism prevails at high driving force. The observed mechanistic switch has major implications for the understanding and control of the water oxidation reaction on heterogeneous catalysts.

INTRODUCTION

Intense research on the water oxidation catalyst (WOC) center in photosystem II (PSII) over the last decades has revealed deep insights on the mechanisms by which mother Nature liberates electrons and protons from H_2O, two critical ingredients for downstream reactions such as CO_2 reduction and N_2 fixation.[1,2] This knowledge has propelled research on using molecular catalysts to oxidize water, and impressive progress has been made in terms of catalyst performance as measured by turn-over frequencies (TOFs) and turn-over numbers (TONs).[3,4] From a technological development perspective, there is a strong incentive to carry out the reaction on heterogeneous catalysts, especially on those of low-cost and outstanding stability. Indeed, recent years have witnessed a surge of such research activities.[5,6,7,8,9,10,11] Despite the apparent variety of these catalysts, they share important commonalities in the chemical mechanisms. For instance, it is generally believed that the reaction proceeds through a series of proton-coupled electron transfer (PCET) steps that lead to the formation of relatively stable M=O (where M represents an active metal center) intermediates.[12,13] It is also agreed upon that the subsequent O-O bond formation is of critical importance to the overall reaction.[14] The details of the O-O formation and the subsequent steps, however, have been the subject of diverging views. At least two possible pathways have been proposed and supported.[15,16,17,18] One involves direct nucleophilic attack of water, followed by O_2 release and regeneration of the catalyst. In the literature, this mechanism is referred to as water nucleophilic attack (WNA, Figure 1, right pathway).[4,15] The other involves the coupling of two metal-oxo intermediates followed by

The Bigger Picture

As the first step in natural photosynthesis, the oxidation of water is of paramount importance. It liberates electrons and protons that are required for downstream reactions such as CO_2 and N_2 reduction. Substantial research efforts have been devoted to understanding and, ultimately, performing this reaction at high efficiency with low-cost, long-lasting catalysts. Exciting progress notwithstanding, much remains poorly understood about the reaction, especially when it is carried out on heterogeneous catalysts. A key elementary step of the water oxidation reaction is the formation of the O-O bond. Herein, we report a potential-induced switch of the O-O bond forming mechanism on Co-oxide-based catalysts. This mechanistic insight is expected to help advance the design of efficient water oxidation catalysts.

O_2 release, which is referred to as intramolecular oxygen coupling (IMOC, Figure 1, left pathway).[15]

For Ir- and Ru-based molecular catalysts, density-functional theory (DFT) calculations predicted that the IMOC pathway dominates at low overpotentials, whereas the WNA pathway becomes accessible at higher overpotentials.[17,19] The two pathways were also predicted to be competitive on a heterogenized dinuclear Ir oxide cluster.[17] With optical pump-probe spectroscopy, Cuk et al. monitored the microsecond decay of oxyl (Ti-O•) and bridge (Ti-O•-Ti) intermediates on $SrTiO_3$ photoelectrodes.[18] They found that the two species decay with distinct reaction rates on a microsecond timescale. It was suggested that Ti-O•s convert to Ti-O-O-Ti by dimerization (IMOC pathway) and Ti-O•-Ti converts to Ti-OOH by nucleophilic attack of water (WNA pathway). Furthermore, it was found that the relative predominance of the two pathways was controlled by the ionic strength of the electrolyte, with the WNA pathway dominating at low ionic strength. However, how the relative predominance of these mechanisms depends on the applied electrode potential has not been investigated in experiments. Herein, we address this central question.

Inspiration on how to further this understanding could be drawn from progress made in molecular WOCs-based studies. To discern different pathways for the water oxidation reaction by molecular catalysts, researchers have resorted to a strategy of correlating the reaction rate with the catalyst concentrations.[4] With the help of additional experiments such as isotope labelling, significant knowledge has been gained.[20,21,22] Similar approaches are challenging to implement for heterogeneous catalysts, however, because the active sites, including their structures and densities, are often poorly defined on a heterogeneous catalyst. The challenge could be circumvented using clever experimental designs. For instance, Durrant et al. have identified a change of reaction orders relative to the hole concentration from the first to the third order on Fe_2O_3 using photoinduced absorption spectroscopy.[23] Frei et al. have succeeded in observing both the metal-oxo, and superoxo species, using an infrared spectroscopy technique.[13] In both studies, different reaction mechanisms were proposed for different light intensities. Nevertheless, due to the lack of detailed information on the active centers, particularly their density under different conditions, it remains difficult to directly corroborate these early observations for an unambiguous understanding of water oxidation on heterogeneous catalysts. While it is possible to address this challenge by synthesizing heterogeneous catalysts with well-defined active centers, as has been demonstrated recently by others and us,[24,25] the catalyst library remains limited, and significant work is needed before the values of such catalysts can be materialized. An alternative approach is to study how the reaction kinetics changes as a function of water activity, which is the main strategy for this present work.

To appreciate the significance of this strategy, it helps to examine the proposed WNA and IMOC pathways on a heterogeneous Co phosphate (Co-Pi) catalyst (Figure 1). Prior studies have suggested that the initial electron/proton transfer steps (vertical arrow in the center) are fast in comparison to the O-O formation. Therefore, these steps are quasi-equilibrated, whereas O-O formation limits the rate of the reaction. From the oxidized state of the catalyst shown on the bottom of the scheme, the water oxidation process can proceed through two distinct pathways: The WNA pathway involves a water molecule within the electric double layer in the rate-determining O-O forming step (right arrow). By contrast, the IMOC pathway only involves surface species in the rate-determining step (RDS) (left arrow). On the basis of this simplified mechanistic picture, the water oxidation reaction is expected to be (pseudo) first order in the water activity when proceeding through the WNA pathway, whereas it is (pseudo) zeroth order when proceeding through the IMOC pathway. It is, therefore, possible to discern the reaction mechanisms even without detailed knowledge of the active centers by altering the water activity, which has not been investigated previously.

The problem is now reduced to how to alter water activity in a water oxidation reaction. Indeed, most prior studies on this subject have treated water as a substrate of invariant activity, such that it was excluded in most kinetic considerations.[26,27] Only recently did we see advances where the water activity could be suppressed significantly in aqueous solutions.[28,29,30] The so-called "water-in-salt" electrolyte containing high concentrations of

salts (e.g., up to 21 m (mole per kg of H_2O)) represents one such system. The strong solvation effect of the high-concentration ions renders its H_2O behaviors drastically different from those in bulk H_2O. It becomes possible to perform water oxidation reactions in an aqueous system where the water activity is no longer unity. We are, therefore, offered an opportunity to test the hypothesis proposed in the previous paragraph. That is, we expect a different sensitivity of the kinetics on the water activity for different mechanisms.

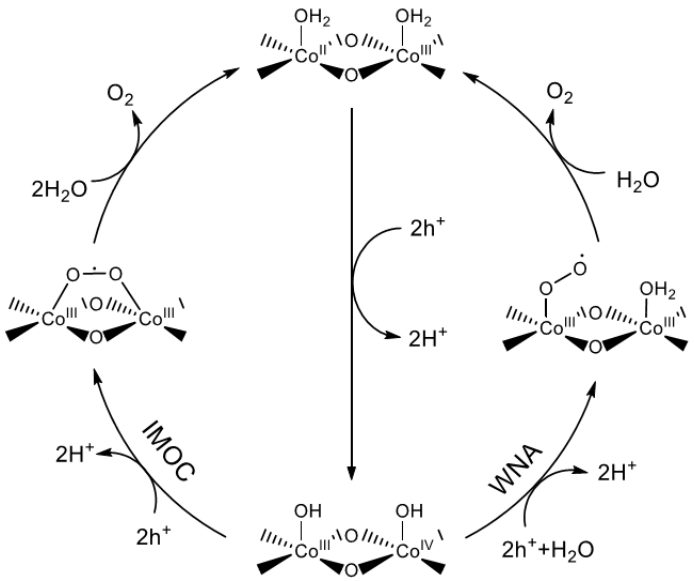

Figure 1. Proposed water oxidation mechanisms by heterogeneous Co phosphate (Co-Pi) catalysts. Two possibilities have been proposed, the intramolecular oxygen coupling pathway (IMOC, left) and the water nucleophilic attack route (WNA, right).

To prove this concept, we have chosen Co-oxide-based catalysts as a study platform because they represent a class of most studied heterogeneous WOCs, with Co phosphate (Co-Pi) receiving arguably the most attention. A broad knowledge base has already been generated.[15,27,31,32,33,34,35,36] For example, the coordination environment of Co has been identified by a suite of spectroscopic techniques.[34] That the O-O formation is the RDS has been supported by numerous studies.[15,27,31,32,35,36] Both WNA and IMOC mechanisms have been proposed and supported by either experimental or computational studies for this catalyst.[15,32,35,36,37,38,39] Herein, we report the new observation of a switch from the IMOC pathway at low applied potentials to the WNA mechanism at high applied potentials.

RESULTS AND DISCUSSION

Detection of water oxidation intermediates

Prior studies have shown that various implementations of infrared and surface-enhanced Raman spectroscopies are powerful probes of water oxidation intermediates.[12,13,18,40,41,42,43,44,45,46,47] To examine the mechanistic proposal (Figure 1), we employed surface-enhanced infrared absorption spectroscopy (SEIRAS) in the attenuated total internal reflection (ATR) geometry. In SEIRAS-ATR, the surface plasmon resonance of rough metal films locally enhances the evanescent field, rendering the technique sensitive of sub-monolayers of species adsorbed on the electrode.[48] With this work, we establish SEIRAS-ATR as a new tool for probing water oxidation intermediates on metal oxide catalysts. For this purpose, we first electrochemically deposited a thin layer of CoOOH[31] onto a chemically deposited Au thin film (CoOOH-Au)[49] on a micro-machined Si-ATR crystal,[50] which affords high infrared transparency below 1200 cm^{-1}. A scheme of the setup

is shown in Figure S1 in the Supplementary information (SI). Here for SEIRAS-ATR, CoOOH but not Co-Pi was employed as the prototypical catalyst because the latter would greatly complicate the interpretation of the IR spectra in the 1000 cm^{-1} region due to the phosphate anion and its response to the applied potentials. As will be discussed in details later in this work, the electrochemical behaviors of CoOOH are comparable to Co-Pi. It also features structurally similar active sites and the same cobalt oxidation states under water oxidation conditions as Co-Pi.[31,51] The CoOOH-Au film exhibits a large activity for water oxidation in comparison with the Au substrate (Figure S2).

Figure 2 shows the steady-state spectra of the CoOOH-Au electrode in 0.1 M potassium phosphate (KPi) in D_2O, H_2O, and $H_2{}^{18}O$. The absorbance was calculated according to Absorbance = -log(*S*/*R*), where *S* and *R* refer to the sample and reference spectra respectively taken at 2.21 V and 1.61 V. Unless otherwise noted, all potentials in this work are relative to the reversible hydrogen electrode (RHE). The spectrum in the D_2O-based electrolyte also exhibited a band centered at 1,014 cm^{-1} (at 2.21 V; Figure 2a). The intensity of this band increased with the increasing applied potentials (Figure S3), suggesting that it is due to a water oxidation intermediate. To assign the band to a water oxidation intermediate, we carried out the following control experiments: First, to exclude the possibility that the band (1,014 cm^{-1}) arises from a phosphate species in the solution, we confirmed the band also appears when the electrolyte is 0.1 M KCl D_2O (Figure S4). Second, the band is absent on a Au electrode without the CoOOH film (Figure S4).

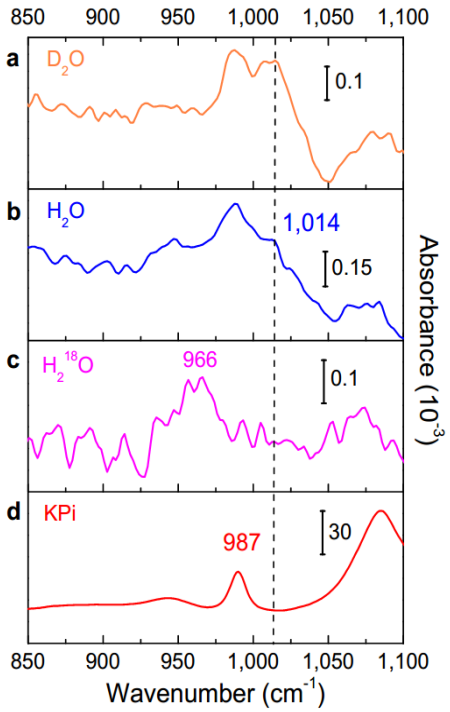

Figure 2. Observation of a superoxo intermediate by SEIRAS-ATR on a CoOOH-Au electrode. Spectra collected on electrodes in contact with 0.1 M solutions of KPi in: (a) D_2O, (b) H_2O, and (c) $H_2{}^{18}O$ at a sample potential of 2.21 V. A spectrum at 1.61 V served as a reference spectrum. The band of the superoxo species is centered at 1,014 cm^{-1} in the presence of D_2O and H_2O and occurs at 966 cm^{-1} in the presence of $H_2{}^{18}O$. All other spectral changes are attributed to KPi. (d) Spectrum of a bulk KPi solution.

These observations strongly suggest that the band centered at 1,014 cm^{-1} is a water oxidation intermediate on CoOOH-Au. According to the proposed mechanism, this spectral feature can be associated with either Co-O-O•-Co from the IMOC pathway or Co-

O-O• or Co-O-OH from the WNA pathway (Figure 1). To further assign this band, we conducted isotopic labelling experiments with H_2O and $H_2{}^{18}O$. The lack of isotopic shift when the solvent is switched from D_2O to H_2O implies that the vibrational mode of the species does not involve a hydrogen atom (Figure 2b). Upon switching to the $H_2{}^{18}O$ electrolyte, this band shifts to 966 cm^{-1} (Figure 2c). The 48 cm^{-1} difference (from 1,014 to 966 cm^{-1}) indicates that the intermediate involves an O-containing motif. These experimental observations support the conclusion that the 1,014 cm^{-1} band is associated with the superoxide intermediates (Co-O-O•-Co or Co-O-O•).[13,42,52] The other possible water oxidation intermediate, hydroperoxide (Co-O-OH), would feature characteristic bands in the 740-920 cm^{-1} region.[42,47,53,54,55] Due to the absorption by the H_2O librational mode, the signals were too weak to be discernable in that spectral range. The other bands in the spectra in Figure 2a-c are due to the enrichment and depletion of electrolyte phosphate species at the interface with changes in applied potential. The spectrum of a bulk KPi solution is shown in Figure 2d. Duplicate experiments confirm the reproducibility of the spectroscopic results (Figure S5). Taken together, this set of experiments demonstrates the utility of the SEIRAS-ATR technique for the detection of water oxidation intermediates. Importantly, the result confirms the presence of a superoxo species, consistent with the mechanistic proposal (Figure 1). Future research should be directed to further distinguish between Co-O-O•-Co and Co-O-O•.

Electrochemical characterization with varying water activities

To further probe the mechanisms as shown in Figure 1, we monitored the electrochemical water oxidation current as a function of electrode potential in water-in-salt electrolytes of varying water activities. As noted above, different reaction orders with respect to water activity are expected from the two competing mechanisms: A (pseudo) first-order dependence on H_2O activity (a_w) is expected for the WNA route, whereas a (pseudo) zeroth-order dependence on a_w is expected for the IMOC pathway. In a practical electrochemical system, the dependence of the kinetics on a_w is likely more complicated because of a number of other factors, including the participation of H_2O as a solvent; these potential complications notwithstanding, the value of quantitatively analyzing the reaction rates as a function of water activity becomes obvious.

Figure 3 compares the steady-state electrochemical current densities due to the oxidation of water on Co-Pi in contact with 0.1 M KPi containing 0, 2, 4, and 7 m $NaNO_3$. The corresponding water activities are shown in the legend and were calculated on the basis of empirical equations.[56] These values describe the activity of bulk water in these water-in-salt electrolytes. We caution that the activity of water at the electrocatalytic interface may be different from those values. Nevertheless, the activities of interfacial water are expected to qualitatively follow the same trend with increasing water-in-salt concentration. All electrolytes were at neutral pH and were stirred during measurements, which were carried out on electrodeposited Co-Pi on fluorine-doped tin oxide (FTO) substrates in a single-compartment electrochemical cell. The potential window was carefully chosen so as to avoid mass transport limitations (i.e., >1.71 V) or large experimental errors due to low current densities (i.e., <1.62 V). Details of the data collection protocol are given in the SI, and a representative data set is shown in Figure S6. As shown, with increasing molality of $NaNO_3$ and, hence, the decreasing a_w, the current density of water oxidation is increasingly suppressed. A similar trend was observed for CoOOH (Figure S7), suggesting that the observed trend is a more general feature of cobalt oxide-based catalysts. This finding further corroborates our assertion made above that CoOOH is an appropriate alternative model system for Co-Pi.

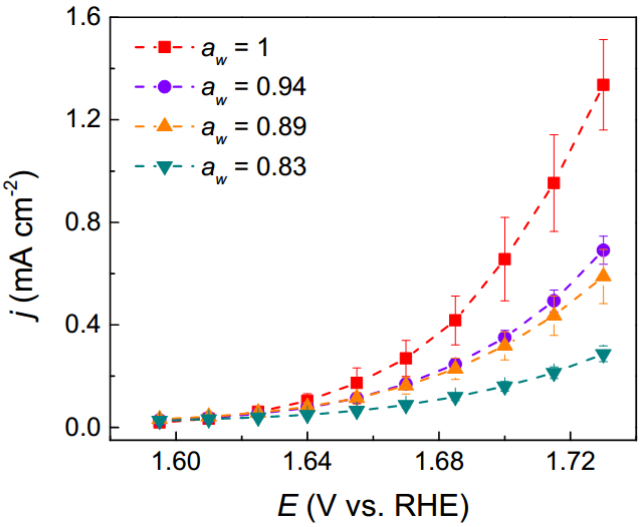

Figure 3. Suppression of the current density due to the water oxidation reaction on Co-Pi when aw was decreased from 1 to 0.83. The water activity was altered by setting the $NaNO_3$ concentration in a 0.1 M KPi buffer at neutral pH to 0 m, 2 m, 4 m, 7 m. The data were collected on a Co-Pi film on an FTO substrate under steady-state conditions and under stirring of the electrolyte. The data were derived from an average of three independent experiments for each a_w. Error bars denote the standard deviation of three individual measurements. The potential was corrected for the *iR*-drop. Further experimental details are provided in the SI.

The observed suppression of the water oxidation reaction could arise from a number of different physical phenomena. First, to test if the catalyst undergoes irreversible structural changes in the different electrolytes, we recorded the CVs of the same Co-Pi electrode in 0.1 M KPi before and after collection of 3 cycles of CVs in the four electrolytes (of molalities 0, 2, 4, 7 m). As shown in Figure S8, the CVs in 0.1 M KPi before and after catalysis in the water-in-salt electrolytes overlap. These data suggest that no irreversible structural changes of the catalyst occur during water oxidation in the water-in-salt electrolytes.

Second, to test if the mass transport of water to the electrode limits the reaction rate at high salt concentrations, we collected the steady-state electrochemical current densities of a Co-Pi-coated Pt rotating disk electrode (RDE) at rotation rates of 2,000 rpm (Figure S9) and 0 rpm (Figure S10). Comparison of the two figures reveals that the recorded current densities on the RDE exhibit the same trend with increasing salt concentration, irrespective of the rotation rate. Moreover, as demonstrated in Table S1, the increase in the thickness of the stagnant layer with electrolyte concentration is expected to be small. Collectively, these results suggest that the suppression of the water oxidation reaction is not caused by limited mass transport of water to the electrode.

Third, at high concentrations of $NaNO_3$, nitrate anions are expected to limit the enrichment of phosphate anions in the electric double layer with increasing potential. As a result, the pH buffer capacity at the electrocatalytic interface might decrease with increasing $NaNO_3$ concentration. Changes in the pH in the vicinity of the electrode (local pH) could impact the reaction rate and mechanism.[27,57] To exclude local pH effects as a possible reason for the reactivity trends with increasing $NaNO_3$ concentration, we carried out three different control experiments: (1) We monitored the electrochemical current density as a function of solution pH at a fixed (absolute) electrode potential. As shown in Figures S11-S13, the pH-dependence of the current density was independent of the rotation rate of the RDE. (2) We carried out galvanostatic titration experiments. The potential shows an approximately Nernstian shift of 60 mV/pH for all electrolytes (Figures S11-S13). (3) We varied the concentration of KPi in the electrolytes containing 4 and 7 m $NaNO_3$. As shown in Figure

S14, the potential-dependence of the reaction rate is insensitive to the concentration of KPi. Taken together, these control experiments suggest that the local pH does not significantly depend on the concentration of $NaNO_3$.

Fourth, to test if nitrate anions block catalytic sites, we recorded the electrochemical current density as a function of potential in 7 m $NaClO_4$. Perchlorate typically does not chemisorb on electrodes.[58] As shown in Figure S15, the impact of 7 m $NaClO_4$ on the current density is similar to that of 7 m $NaNO_3$. This result indicates that nitrate anions do not block catalytic sites of Co-Pi.

Fifth, alkali metal cations are known to influence the rate of the water oxidation reaction on various electrocatalysts.[59,60,61,62,63] In the case of Ni oxyhydroxides, intercalated electrolyte cations have been proposed to stabilize reaction intermediates.[60,62] To test if the catalytic activity is affected by the identity of the cation, we conducted additional control experiments in 2 m KNO_3. As shown in Figure S16, the current modulation ratio virtually overlaps with the one obtained in 2 m $NaNO_3$ (higher concentrations of KNO_3 could not be tested because of the lower solubility of that salt relative to $NaNO_3$). This result is consistent with earlier work[64] showing that the substitution of K^+ in Co-Pi by Na^+ has no significant impact on the catalytic activity of this catalyst. On the basis of this finding and our observation that the catalytic activity of Co-Pi is retained after a sequence of CVs in three water-in-salt electrolytes (Figure S8), we can exclude the incorporation of Na^+ into the Co-Pi film as the origin of the change in catalytic activity with increasing electrolyte concentration. Cations can also influence an electrocatalytic process by altering the properties of the electric double layer in a number of distinct ways,[65] which are not fully understood to date. One of the principal ways in which cations can impact the catalytic activity is by altering the structure and dynamics of water at the interface.[63,65] This possibility is included in our interpretation of these results in terms of the decreasing activity of water with increasing concentration of the water-in-salt electrolytes.

Sixth, to exclude possible impurities, e.g. Fe incorporation[66] in OER differently with increasing salt concentration, we performed CV tests in electrolytes with reagent grade and trace metal grade salts. As shown in Figure S17, the same water oxidation activity was observed in both electrolytes.

Lastly, to test if the electrochemical currents arise from the oxidation of water to molecular oxygen, we conducted gas chromatography measurements. Figure S18 shows that O_2 is produced with near-unity Faradaic efficiency. This measurement demonstrates that (1) other possible oxidation products (such as H_2O_2) are not produced in appreciable amounts and (2) parasitic chemical reactions (such as the oxidation of nitrate) do not occur.

Taken as a whole, this set of results indicates that the observed suppression of the water oxidation reaction is most likely due to the decrease of water activity (a_w) from 1 to 0.83 as the concentration of $NaNO_3$ increases from 0 to 7 m.

To further analyze the data shown in Figure 3, we plotted the ratio of the current density at a_w =1 over that at a_w =0.83 at different potentials (Figure 4). This ratio quantifies the extent to which the reaction rate is modulated by the water activity. It is clear that the impact of the water activity strongly depends on the electrode potential: At 1.71 V, the rate is suppressed by a factor of ≈4.3. By contrast, at a potential of 1.615 V, the modulation factor is only ≈1.2, indicating that the rate of the reaction is less sensitive to the change in water activity at that potential. Identical trends were obvious for the other a_w's (i.e., 0.94 and 0.89), albeit with different magnitudes.

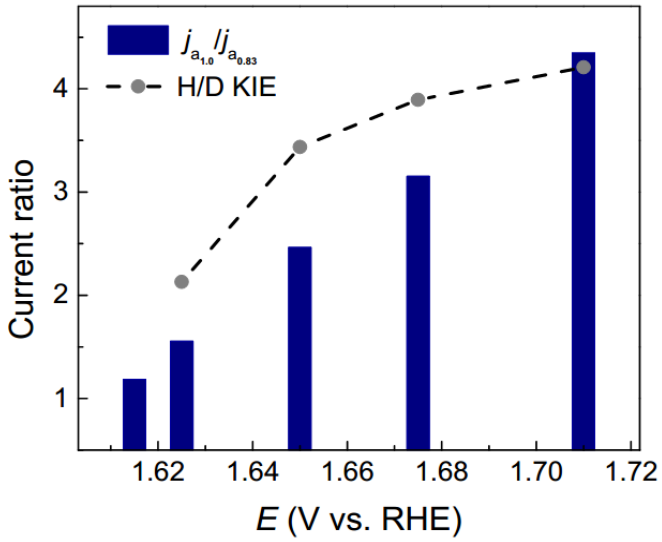

Figure 4. Potential-dependence of the current modulation ratio for different water activities and solvents. $j_{a1.0}/j_{a0.83}$ is the ratio of the water oxidation current densities on the Co-Pi catalyst observed in electrolytes with water activities of 1 and 0.83. The ratio $j_{a1.0}/j_{a0.83}$ was calculated from the data in Figure 3. H/D refers to the ratio of the current densities of the Co-Pi catalyst in 0.1 M KPi in H_2O and D_2O. The potential was corrected for the *iR*-drop.

That the reaction rate is suppressed by up to a factor of 4.3 by an a_w change from 1 to 0.83 at 1.71 V strongly suggests that H_2O is involved in the rate-determining step at that potential. Conversely, for the same a_w, the modulation is close to unity at 1.615 V, indicating that H_2O involvement in the rate-determining step is less likely. Taken as a whole, the data suggest that a mechanistic switch occurs between 1.615 V and 1.71 V. A possible mechanistic switch that is consistent with our observations is the transition from the IMOC pathway ((pseudo) zeroth-order in a_w) to the WNA route ((pseudo) first-order in a_w) as the electrode potential is increased from 1.615 to 1.71 V.

To corroborate further this assertion, we measured the steady-state current density on the FTO-supported Co-Pi electrode in 0.1 M KPi in heavy water (D_2O) as a function of electrode potential. The ratio of the current density of the corresponding measurement in light water over that in heavy water is the apparent kinetic isotope effect (KIE). The apparent KIE is close to 2 at 1.625 V and increases to ≈4.2 as the potential is tuned to 1.71 V. Because the IMOC pathway does not involve water in the rate-determining step, we expect the rate of the reaction to be insensitive to H/D substitution. By contrast, the WNA involves a water molecule in the rate-determining step. Therefore, a dependence of the rate on the isotope of hydrogen is expected. Collectively, the KIE measurements further corroborate our notion that the mechanism switches from the IMOC route to the WNA pathway with increasing potential.

We note that the interpretation of KIE effects can be highly complex. For example, a similar KIE dependence on potential might be explained by a switch of the oxidized substrates from OH^- to H_2O, as has been reported by Zhao et al. on Fe_2O_3.[67] That mechanism, however, is not applicable to the Co-Pi catalyst because OH^- is unlikely to be the oxidized substrate at pH 7. Furthermore, Hammes-Schiffer et al. demonstrated that the relative contributions that specific reactant/product vibronic states make to the current density are dependent on the isotope.[68] They showed that this effect could give rise to a potential-dependence of the KIE. While we cannot fully rule out that such effects contribute to the potential-dependence of the KIE in the present case, the corroboration between the KIE data and the potential-dependent impact of the water activity on the reaction rate supports the conclusion of a potential-induced switch from the IMOC

mechanism to the WNA pathway with increasing potential. A KIE on the WNA pathway was also reported by Cuk et al. during the photocatalytic oxidation of water on $SrTiO_3$.[18]

As far as the KIE effect is concerned, it is noted that Dau and co-workers also found a suppression of the water oxidation reaction in D_2O relative to that in H_2O.[32] Their electrokinetic results were similar to those reported herein. However, they interpreted these data differently. Specifically, the authors found that the redox-potential of the pre-equilibrium $[Co^{III}\text{-}OH] \leftrightharpoons [Co^{IV}\text{-}O] + H^+ + e^-$ shifts by about 60 mV in the anodic direction upon switching the solvent from H_2O to D_2O. Because galvanostatic measurements for water oxidation in H_2O and D_2O show a similar shift, they suggested that the suppression of the water oxidation reaction is due to the shift in this pre-equilibrium (rather than a KIE on the rate-determining step of the water oxidation reaction). This alternative interpretation could also account for the observed suppression of the water oxidation in D_2O. However, we note that on the basis of the cyclic voltammograms of Co-Pi in H_2O and D_2O (Figure S19), we estimated a shift of ≈28 mV in the Co(II)/Co(III) redox half-wave potential. The relatively small shift in the pre-equilibrium suggests that it may not be the sole reason for the observed dependence of the rate of the water oxidation on the H/D isotope. Most importantly, this interpretation cannot account for the suppression of the current with increasing salt concentration (Figures 3 and 4). As discussed above, our control experiments in which we varied the rotation rate of the RDE (Figures S9-S10), the pH of the electrolyte (Figures S11-S13), and the concentration of KPi (Figure S14) confirm that the buffer capacity is sufficient to maintain the $[Co^{III}\text{-}OH] \leftrightharpoons [Co^{IV}\text{-}O] + H^+ + e^-$ equilibrium in the water-in-salt electrolytes. To further corroborate this notion, we analyzed the Co(II)/Co(III) redox equilibrium of Co-Pi in contact with the water-in-salt electrolytes with cyclic voltammetry. As shown in Figure S20, the Co(II)/Co(III) redox half-wave potential is shifted by only 10-20 mV in the cathodic direction with increasing salt concentration. This small shift indicates the pre-equilibrium is not significantly affected by the presence of water-in-salt electrolytes. Therefore, when the isotope effect results are viewed in the context of the electrokinetic results for the water-in-salt electrolytes, our interpretation provides a cohesive, self-consistent picture, whereas the hypothesis that the shift in the pre-equilibrium can only partly explain the collective results. Although the shift may be a contributing factor, we conclude that it is not the dominating effect.

Rationalization of the Potential-Induced Mechanistic Switch

In the following section, we discuss two possible molecular origins for our proposed potential-induced mechanistic switch. First, we show that the interfacial electric field at the electrocatalyst/electrolyte contact may affect the relative activation barriers of the two pathways, and, thus, the relative weight of each route as the potential is altered. Second, we performed density functional theory (DFT) study of the two routes. These calculations show that only at high potentials does the WNA mechanism become thermodynamically accessible. In a practical system, the two effects may synergistically combine to favor the WNA pathway at high electrode potentials. Next, we first discuss the impact of the interfacial electric field on the activation barriers; then we describe the insights derived from the DFT modeling.

The key distinction between the IMOC and WNA pathways is the involvement of water in the rate-determining step of the latter one (Figure 1). On the basis of this observation, we expect the energetics of the two pathways to exhibit distinct sensitivity to the interfacial electric field. The magnitude of the interfacial electric field of the electric double layer increases as the potential of the electrode is increased. It is well established that electric fields can profoundly impact the rates and selectivity of chemical reactions.[69,70,71,72,73] Reaction intermediates with sufficiently large dipole moments and polarizabilities can interact with the electric fields. As a result of this interaction, the free energy profile of the reaction processes can be altered.[69,70] Nørskov et al. have shown that the impact of electric fields on surface-bound water oxidation intermediates (M-OOH, M-OH, M=O) is typically very small because these species have small dipole moments and polarizabilities.[72] On the basis of these findings, it is likely that the interfacial electric field has negligible impact on the IMOC pathway. Because the rate-determining O-O bond formation step is a chemical step, we expect the principal activation barrier of the IMOC pathway to be independent of the electrode potential. By contrast, because water has a relatively large dipole moment

and polarizability, the orientation and dynamics of water molecules at electrified interfaces may strongly depend on the electrode potential.[73,74,75] It has been suggested the water dynamics and structure at interfaces affect the rates of various electrocatalytic processes, such as water oxidation and reduction.[63,73] Therefore, even though O-O coupling in the WNA as hypothesized in Figure 1 is a chemical step, we expect the activation barrier of this process to depend on the electrode potential: $\Delta G_{WHAA}^{\neq} = \Delta G_{WHAA}^{\neq} - \Delta\vec{\mu} \cdot \vec{E}$, where $\Delta G_{WHAA}^{\neq}$ is the standard chemical free energy of activation in the absence of an electric field; $\Delta\vec{\mu}$ represents the change in the surface dipole when going from the reactant to the activated complex state; and $\vec{E}$ is the interfacial electric field, which depends on the electrode potential. These qualitative considerations show that because of the participation of water in the rate-determining chemical step of O-O bond formation for the WNA mechanism, the activation barrier of this step is a function of electrode potential. Nevertheless, without knowledge of the molecular-level structure of the electrocatalyst/electrolyte interface at the present time, our considerations must remain qualitative in nature at the present stage. Irrespective, this model describes one possible origin of the observed mechanistic switch from the IMOC route to the WNA pathway with increasing potential.

To explore further other possible causes of the potential-induced switch, we studied the energetics of the two pathways with DFT. All calculations were performed with the B3LYP functional and def2-SV(P) and def2-TZVP basis set implemented in the Gaussian 16 software package. Further computational details are provided in the SI. We constructed atomic models on the basis of previous EXAFS[34] and X-ray pair distribution function analysis.[51] The $Co_7O_{24}H_{27}$ cluster has a Co ion surrounded by 6 Co ions at the edge which are connected to the center Co ion by μ_3-O bridges (Figure S21). The energetics of the water oxidation reaction is sensitive to the protonation state of the cluster.[35,36] We considered different protonation states and found that the lowest energy protonation state is a highly symmetric cluster with one side of the μ_3-O being protonated, and each pair of edge Co ions having strong hydrogen bonds between nearby hydroxide and water ligands (Figure S22). The protonation of the hydroxide ligand of the edge Co atoms is energetically unfavorable since it destroys the strong hydrogen bond interaction between OH^- and nearby H_2O. However, the edge OH^- group can be protonated by reducing the corresponding edge Co(III) to Co(II) (Figure S23).

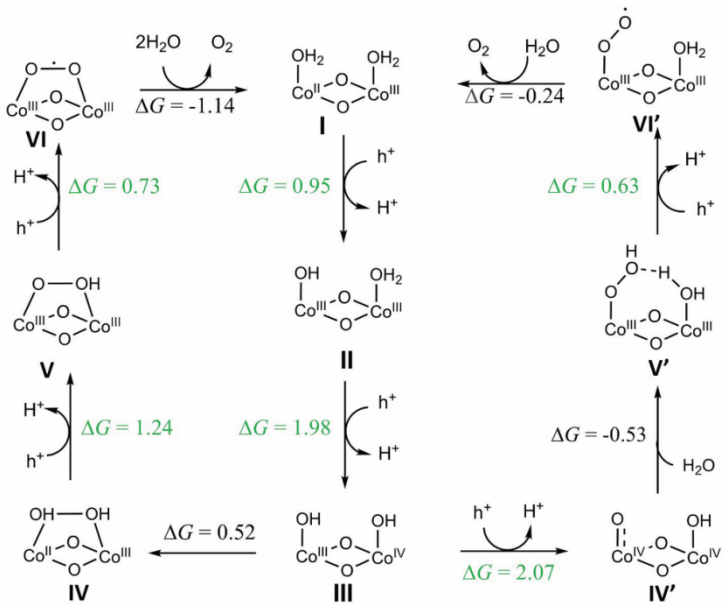

Figure 5. Possible routes of water oxidation suggested by the DFT calculations. Left: the IMOC mechanism under low overpotential (thermodynamically favored pathway); right: the WNA mechanism under high overpotential. The calculated free energy changes

(ΔI) are given in the unit of eV. The numbers shown in green are the free energy changes of electrochemical steps vs. the computed hydrogen electrode.

On the basis of this structural model, we investigate the water oxidation mechanism (Figure 5) starting from the H_2O-Co(II)-(μ-O)$_2$-Co(III)-OH_2 intermediates (I). We note that our computational method overestimates the oxidation potential of Co(III) to Co(IV) by ~0.3 V (Figure S24). All potentials quoted herein are not corrected for this systematic error. The oxidation of Co(II) to Co(III) requires 0.95 V, which is much lower than the applied potential during catalysis. The second oxidation requires 1.98 V to generate intermediate III with one Co oxidized to Co(IV). This oxidation is a metal-center oxidation, consistent with XANES results of the Co-Pi catalyst under catalytic conditions, which suggest a valence of Co great than 3.[34] When the overestimation of the redox potential is accounted for, this intermediate is predicted to be prevalent under water oxidation conditions. Consistent with the prediction, the resting state of the catalyst has been assigned to intermediate III in prior reports.[15,27,31,32,57,76] The hydroxide coordinated to the Co(IV) center in intermediate III has a partial radical character as indicated by a Mulliken spin population of 0.21 (Figure S25). Therefore, the two hydroxides can couple to form hydroperoxide through the IMOC mechanism. Thermodynamically, this pathway is favored over the WNA pathway under low applied potentials. The following two oxidations require low potentials. Therefore, it is fairly easy to form intermediate VI. The release of O_2 and binding of two water molecules complete the catalytic cycle.

Under high applied potential, intermediate III can be further oxidized to form intermediate IV′ with two nearby Co being oxidized to Co(IV). The terminal O atom coordinated to Co(IV) is best described as an oxyl radical since the Mulliken spin population on the O atom is 0.89 (Figure S25), close to 1 for a perfect radical. The intermediate IV′ can react with a water molecule from the solution to form intermediate V′ through the WNA mechanism. The incoming H_2O forms hydroperoxide with the oxyl radical and releases a proton the nearby OH^- group. Intermediate V′ can be further oxidized to intermediate VI′, which releases O_2 and adsorbs a water molecule to complete the catalytic cycle.
We note that both IMOC and WNA mechanisms feature a superoxo intermediate (VI and VI′, respectively). This prediction is consistent with our spectroscopic results, which indicate the presence of a superoxo species. On the basis of the simulated O-O vibrational frequencies (Figure S26) alone, we cannot identify which of the two species gives rise to the vibrational band at 1,014 cm^{-1} (Figure 2). We reserve a more detailed assignment for future investigations.

Although alternative reaction pathways may be available,[36,77] the DFT computations show that (1) the IMOC and WNA pathways are feasible from a thermodynamic perspective and (2) their energetics are consistent with the proposed mechanistic framework (Figure 1) and the interpretation of our electrokinetic results (Figures 3 and 4): At low overpotential, the IMOC pathway predominates, whereas the WNA pathway becomes accessible at high overpotential. Lastly, it is noted that, in line with prior precedence, we only considered the thermodynamics of the pathways.[19,77] The calculation of the activation barriers is complicated by spin-state changes during the conversion of intermediate III to IV. Further, the activation barriers are sensitive to the protonation state of the catalyst, which is a complex function of applied electrode potential and reaction conditions. Fully accounting for these complications will require additional research that is beyond of the scope of the current work.

Taken as a whole, the thermodynamic description of the two pathways and the qualitative considerations of the impact of the interfacial field on the relative magnitude of activation barriers of the O-O bond-forming steps provide strong support for the conclusion of a potential-dependent mechanistic switch. The DFT modeling predicts that a certain threshold potential for the WNA pathway needs to be surpassed before this pathway becomes thermodynamically feasible. In addition, the involvement of water in the rate-determining step may further lower the activation barrier for the O-O bond formation step for the WNA route, leading to a further acceleration of the reaction rate.

Broader Implications

Prior research on homogeneous water oxidation mechanisms has revealed that the 4-proton, 4-electron process of water oxidation can take place on a mononuclear or a dinuclear catalyst. Whether WNA or oxygen-coupling is the preferred mechanism has been at the center of intense studies for the natural photosystem II, as well as for molecular catalysts. In testing the various hypotheses for the reaction mechanisms, researchers mainly relied on kinetic models that depend on the information of key species, such as the concentration of the catalyst and the turn-over frequencies. In principle, the same methodology could be applied for the establishment of a similar knowledge base for heterogeneous water oxidation reactions. However, the lack of knowledge on the detailed information of the catalytically active centers creates a critical challenge for such an approach. Our strategy of probing the kinetics of heterogeneous water oxidation by varying water activities is new. It generates information that permits the verification of hypotheses that are difficult or impossible to obtain by other methods. How the water oxidation reaction proceeds is sensitive to a number of factors, including the local catalytic environment (e.g., the availability of mononuclear, dinuclear or multinuclear active centers), substrate concentration, as well as the driving forces. While our studies suggest that the WNA mechanism is favored at high driving force, we are inspired to understand that in a practical water oxidation system (such as the Oxygen Evolution Catalyst in Photosystem II or in an electrolyzer), both mechanisms may co-exist. The fact that this switch is observed on Co-Pi and CoOOH (Figures S7 and S27) suggests that the potential-induced changes in pathway may be a more general phenomenon of Co-oxide based electrocatalytsts. The dynamic switch of the mechanisms could help to explain how mother Nature ensures the most efficient route for the utilization of solar energy to liberate electrons and protons; it also implies that future designs and optimization of heterogeneous catalysts for large-scale engineering implementations of water oxidation should take into the account of the facile switch of reaction mechanisms. It is noted that the WNA mechanism could proceed through a mononuclear site or a dinuclear site depending on the catalytic conditions.[13,78,79] However, we believe it provides a minor contribution to our study because of the narrow and low overpotential regime investigated, as well as the equivalent involvement of water molecule in the rate-determining step on both sites. Lastly, while we envision that studying water oxidation by varying water activities indeed adds a new dimension to the tool kit, it faces limitations for systems at highly alkaline conditions where OH^- but not H_2O is being oxidized.

In conclusion, this work introduced two key innovations. Using SEIRAS-ATR, we detected a key intermediate corresponding to O-O bond formation in Co-based water oxidation. This information lends support to the proposed mechanisms. By varying water activities, we established a kinetic model that allowed us to verify the two competing mechanisms of water oxidation. It was found that the dinuclear route (i.e., IMOC) is favored at relatively low driving forces, whereas the mononuclear route (i.e., WNA) is preferred at relatively high driving forces. The results contribute significantly to the understanding of water oxidation by heterogeneous catalysts.

EXPERIMENTAL PROCEDURES

Resource Availability

Lead Contact

Further information and requests for resources should be directed to and will be fulfilled by the Lead Contact, Dunwei Wang (dunwei.wang@bc.edu).

Materials Availability

This study did not generate new unique reagents.

Data and Code Availability

This study did not generate any datasets.

SUPPLEMENTAL INFORMATION

Document S1. Materials and Experimental Procedures, Figures S1–S27, Tables S1, and Supplemental References

ACKNOWLEDGMENTS

The work at Boston College is supported by the U.S. Department of Energy (DOE), Office of Science, Office of Basic Energy Sciences, Chemical Sciences, Geosciences, and Biosciences Division (DE-SC0020261). Work at Yale University was supported by the U.S. Department of Energy (DOE), Office of Science, Office of Basic Energy Sciences, Chemical Sciences, Geosciences, and Biosciences Division (DE-FG02-07ER15909). V.S.B. acknowledges the computer time from the National Energy Research Scientific Computing Center (NERSC) and Yale Center for Research Computing (YCRC).

AUTHOR CONTRIBUTIONS

C.L. and Y.W. carried out the electrochemical experiments; J.L. performed the SEIRAS-ATR; K.R.Y. conducted computational studies; J.E.T., Q.D., D.H., and Y.Z. contributed experimentally; Y.W. participated in data analysis and visualization; all authors participated in discussions and the writing of the manuscript; V.S.B., M.M.W., and D.W. co-directed the project.

DECLARATION OF INTERESTS

The authors declare no competing interests.

REFERENCES

1. Shen, J.-R. (2015) The Structure of Photosystem II and the Mechanism of Water Oxidation in Photosynthesis. *Annu. Rev. Plant Biol.*, *66*, 23-48.
2. Vinyard, D. J.; Brudvig, G. W. (2017) Progress Toward a Molecular Mechanism of Water Oxidation in Photosystem II. *Annu. Rev. Phys. Chem.*, *68*, 101-116.
3. Blakemore, J. D.; Crabtree, R. H.; Brudvig, G. W. (2015) Molecular Catalysts for Water Oxidation. *Chem. Rev.*, *115*, 12974-13005.
4. Shaffer, D. W.; Xie, Y.; Concepcion, J. J. (2017) O–O bond formation in ruthenium-catalyzed water oxidation: single-site nucleophilic attack vs. O–O radical coupling. *Chem. Soc. Rev.*, *46*, 6170-6193.
5. Hunter, B. M.; Gray, H. B.; Müller, A. M. (2016) Earth-Abundant Heterogeneous Water Oxidation Catalysts. *Chem. Rev.*, *116*, 14120-14136.
6. Suen, N.-T.; Hung, S.-F.; Quan, Q.; Zhang, N.; Xu, Y.-J.; Chen, H. M. (2017) Electrocatalysis for the oxygen evolution reaction: recent development and future perspectives. *Chem. Soc. Rev.*, *46*, 337-365.
7. Zhang, M.; Frei, H. (2017) Water Oxidation Mechanisms of Metal Oxide Catalysts by Vibrational Spectroscopy of Transient Intermediates. *Annu. Rev. Phys. Chem.*, *68*, 209-231.
8. Yu, Z.-Y.; Duan, Y.; Gao, M.-R.; Lang, C.-C.; Zheng, Y.-R.; Yu, S.-H. (2017) A one-dimensional porous carbon-supported Ni/Mo_2C dual catalyst for efficient water splitting. *Chem. Sci.*, *8*, 968-973.
9. Yu, Z.-Y.; Lang, C.-C.; Gao, M.-R.; Chen, Y.; Fu, Q.-Q.; Duan, Y.; Yu, S.-H. (2018) Ni–Mo–O nanorod-derived composite catalysts for efficient alkaline water-to-hydrogen conversion via urea electrolysis. *Energy Environ. Sci.*, *11*, 1890-1897.
10. Grimaud, A.; Diaz-Morales, O.; Han, B.; Hong, W. T.; Lee, Y.-L.; Giordano, L.; Stoerzinger, K. A.; Koper, M. T. M.; Shao-Horn, Y. (2017) Activating lattice oxygen redox reactions in metal oxides to catalyse oxygen evolution. *Nat. Chem.*, *9*, 457-465.
11. Negahdar, L.; Zeng, F.; Palkovits, S.; Broicher, C.; Palkovits, R. (2019) Mechanistic Aspects of the Electrocatalytic Oxygen Evolution Reaction over Ni–Co Oxides. *ChemElectroChem*, *6*, 5588-5595.
12. Zandi, O.; Hamann, T. W. (2016) Determination of photoelectrochemical water oxidation intermediates on haematite electrode surfaces using operando infrared spectroscopy. *Nat. Chem.*, *8*, 778-783.
13. Zhang, M.; de Respinis, M.; Frei, H. (2014) Time-resolved observations of water oxidation intermediates on a cobalt oxide nanoparticle catalyst. *Nat. Chem.*, *6*, 362-367.
14. Rosenthal, J.; Nocera, D. G. (2007) Role of proton-coupled electron transfer in O–O bond activation. *Acc. Chem. Res.*, *40*, 543-553.
15. Ullman, A. M.; Brodsky, C. N.; Li, N.; Zheng, S.-L.; Nocera, D. G. (2016) Probing Edge Site Reactivity of Oxidic Cobalt Water Oxidation Catalysts. *J.*

Am. Chem. Soc., *138*, 4229-4236.

16. Romain, S.; Vigara, L.; Llobet, A. (2009) Oxygen–Oxygen Bond Formation Pathways Promoted by Ruthenium Complexes. *Acc. Chem. Res.*, *42*, 1944-1953.
17. García-Melchor, M.; Vilella, L.; López, N.; Vojvodic, A. (2016) Computationally Probing the Performance of Hybrid, Heterogeneous, and Homogeneous Iridium-Based Catalysts for Water Oxidation. *ChemCatChem*, *8*, 1792-1798.
18. Chen, X.; Aschaffenburg, D. J.; Cuk, T. (2019) Selecting between two transition states by which water oxidation intermediates decay on an oxide surface. *Nat. Catal.*, *2*, 820-827.
19. Craig, M. J.; Coulter, G.; Dolan, E.; Soriano-López, J.; Mates-Torres, E.; Schmitt, W.; García-Melchor, M. (2019) Universal scaling relations for the rational design of molecular water oxidation catalysts with near-zero overpotential. *Nat. Commun.*, *10*, 4993.
20. Matheu, R.; Ertem, M. Z.; Gimbert-Suriñach, C.; Sala, X.; Llobet, A. (2019) Seven Coordinated Molecular Ruthenium–Water Oxidation Catalysts: A Coordination Chemistry Journey. *Chem. Rev.*, *119*, 3453-3471.
21. Duan, L.; Bozoglian, F.; Mandal, S.; Stewart, B.; Privalov, T.; Llobet, A.; Sun, L. (2012) A molecular ruthenium catalyst with water-oxidation activity comparable to that of photosystem II. *Nat. Chem.*, *4*, 418-423.
22. Romain, S.; Bozoglian, F.; Sala, X.; Llobet, A. (2009) Oxygen–Oxygen Bond Formation by the Ru-Hbpp Water Oxidation Catalyst Occurs Solely via an Intramolecular Reaction Pathway. *J. Am. Chem. Soc.*, *131*, 2768-2769.
23. Le Formal, F.; Pastor, E.; Tilley, S. D.; Mesa, C. A.; Pendlebury, S. R.; Grätzel, M.; Durrant, J. R. (2015) Rate Law Analysis of Water Oxidation on a Hematite Surface. *J. Am. Chem. Soc.*, *137*, 6629-6637.
24. Zhao, Y.; Yan, X.; Yang, K. R.; Cao, S.; Dong, Q.; Thorne, J. E.; Materna, K. L.; Zhu, S.; Pan, X.; Flytzani-Stephanopoulos, M.; Brudvig, G. W.; Batista, V. S.; Wang, D. (2018) End-On Bound Iridium Dinuclear Heterogeneous Catalysts on WO_3 for Solar Water Oxidation. *ACS Cent. Sci.*, *4*, 1166-1172.
25. Zhao, Y.; Yang, K. R.; Wang, Z.; Yan, X.; Cao, S.; Ye, Y.; Dong, Q.; Zhang, X.; Thorne, J. E.; Jin, L.; Materna, K. L.; Trimpalis, A.; Bai, H.; Fakra, S. C.; Zhong, X.; Wang, P.; Pan, X.; Guo, J.; Flytzani-Stephanopoulos, M.; Brudvig, G. W.; Batista, V. S.; Wang, D. (2018) Stable iridium dinuclear heterogeneous catalysts supported on metal-oxide substrate for solar water oxidation. *Proc. Natl. Acad. Sci.*, *115*, 2902-2907.
26. Wuttig, A.; Yoon, Y.; Ryu, J.; Surendranath, Y. (2017) Bicarbonate Is Not a General Acid in Au-Catalyzed CO_2 Electroreduction. *J. Am. Chem. Soc.*, *139*, 17109-17113.
27. Surendranath, Y.; Kanan, M. W.; Nocera, D. G. (2010) Mechanistic Studies of the Oxygen Evolution Reaction by a Cobalt-Phosphate Catalyst at Neutral pH. *J. Am. Chem. Soc.*, *132*, 16501-16509.
28. Suo, L.; Borodin, O.; Gao, T.; Olguin, M.; Ho, J.; Fan, X.; Luo, C.; Wang, C.; Xu, K. (2015) "Water-in-salt" electrolyte enables high-voltage aqueous lithium-ion chemistries. *Science*, *350*, 938-943.
29. Dong, Q.; Yao, X.; Zhao, Y.; Qi, M.; Zhang, X.; Sun, H.; He, Y.; Wang, D. (2018) Cathodically Stable Li-O_2 Battery Operations Using Water-in-Salt Electrolyte. *Chem*, *4*, 1345-1358.
30. Dong, Q.; Zhang, X.; He, D.; Lang, C.; Wang, D. (2019) Role of H_2O in CO_2 Electrochemical Reduction As Studied in a Water-in-Salt System. *ACS Cent. Sci.*, *5*, 1461-1467.
31. Bergmann, A.; Jones, T. E.; Martinez Moreno, E.; Teschner, D.; Chernev, P.; Gliech, M.; Reier, T.; Dau, H.; Strasser, P. (2018) Unified structural motifs of the catalytically active state of Co(oxyhydr)oxides during the electrochemical oxygen evolution reaction. *Nat. Catal.*, *1*, 711-719.
32. Pasquini, C.; Zaharieva, I.; Gonzalez-Flores, D.; Chernev, P.; Mohammadi, M. R.; Guidoni, L.; Smith, R. D. L.; Dau, H. (2019) H/D isotope effects reveal factors controlling catalytic activity in Co-based oxides for water oxidation. *J. Am. Chem. Soc.*, *141*.
33. Kanan, M. W.; Nocera, D. G. (2008) In Situ Formation of an Oxygen-Evolving Catalyst in Neutral Water Containing Phosphate and Co^{2+}. *Science*, *321*, 1072-1075.
34. Kanan, M. W.; Yano, J.; Surendranath, Y.; Dincă, M.; Yachandra, V. K.; Nocera, D. G. (2010) Structure and Valency of a Cobalt–Phosphate Water Oxidation Catalyst Determined by in Situ X-ray Spectroscopy. *J. Am. Chem. Soc.*, *132*, 13692-13701.
35. Li, X.; Siegbahn, P. E. M. (2013) Water Oxidation Mechanism for Synthetic Co–Oxides with Small Nuclearity. *J. Am. Chem. Soc.*, *135*, 13804-13813.
36. Wang, L.-P.; Van Voorhis, T. (2011) Direct-Coupling O_2 Bond Forming a Pathway in Cobalt Oxide Water Oxidation Catalysts. *J. Phys. Chem. Lett.*, *2*, 2200-2204.
37. McAlpin, J. G.; Stich, T. A.; Casey, W. H.; Britt, R. D. (2012) Comparison of cobalt and

manganese in the chemistry of water oxidation. *Coord. Chem. Rev.*, *256*, 2445-2452.
38. Mattioli, G.; Giannozzi, P.; Amore Bonapasta, A.; Guidoni, L. (2013) Reaction Pathways for Oxygen Evolution Promoted by Cobalt Catalyst. *J. Am. Chem. Soc.*, *135*, 15353-15363.
39. Risch, M.; Ringleb, F.; Kohlhoff, M.; Bogdanoff, P.; Chernev, P.; Zaharieva, I.; Dau, H. (2015) Water oxidation by amorphous cobalt-based oxides: in situ tracking of redox transitions and mode of catalysis. *Energy Environ. Sci.*, *8*, 661-674.
40. Nakamura, R.; Nakato, Y. (2004) Primary Intermediates of Oxygen Photoevolution Reaction on TiO_2 (Rutile) Particles, Revealed by in Situ FTIR Absorption and Photoluminescence Measurements. *J. Am. Chem. Soc.*, *126*, 1290-1298.
41. Pavlovic, Z.; Ranjan, C.; van Gastel, M.; Schlögl, R. (2017) The active site for the water oxidising anodic iridium oxide probed through in situ Raman spectroscopy. *Chem. Commun.*, *53*, 12414-12417.
42. Sivasankar, N.; Weare, W. W.; Frei, H. (2011) Direct Observation of a Hydroperoxide Surface Intermediate upon Visible Light-Driven Water Oxidation at an Ir Oxide Nanocluster Catalyst by Rapid-Scan FT-IR Spectroscopy. *J. Am. Chem. Soc.*, *133*, 12976-12979.
43. Zhang, Y.; Zhang, H.; Liu, A.; Chen, C.; Song, W.; Zhao, J. (2018) Rate-Limiting O–O Bond Formation Pathways for Water Oxidation on Hematite Photoanode. *J. Am. Chem. Soc.*, *140*, 3264-3269.
44. Liu, H.; Frei, H. (2020) Observation of O–O Bond Forming Step of Molecular Co_4O_4 Cubane Catalyst for Water Oxidation by Rapid-Scan FT-IR Spectroscopy. *ACS Catal.*, *10*, 2138-2147.
45. Chen, X.; Choing, S. N.; Aschaffenburg, D. J.; Pemmaraju, C. D.; Prendergast, D.; Cuk, T. (2017) The Formation Time of Ti–O• and Ti–O•–Ti Radicals at the n-$SrTiO_3$/Aqueous Interface during Photocatalytic Water Oxidation. *J. Am. Chem. Soc.*, *139*, 1830-1841.
46. Herlihy, D. M.; Waegele, M. M.; Chen, X.; Pemmaraju, C. D.; Prendergast, D.; Cuk, T. (2016) Detecting the oxyl radical of photocatalytic water oxidation at an n-$SrTiO_3$/aqueous interface through its subsurface vibration. *Nat. Chem.*, *8*, 549-555.
47. Yeo, B. S.; Bell, A. T. (2011) Enhanced activity of gold-supported cobalt oxide for the electrochemical evolution of oxygen. *J. Am. Chem. Soc.*, *133*, 5587-5593.
48. Osawa, M.: Surface-Enhanced Infrared Absorption. In *Near-Field Optics and Surface Plasmon Polaritons*; Kawata, S., Ed.; Springer Berlin Heidelberg: Berlin, Heidelberg, 2001; pp 163-187.
49. Miyake, H.; Ye, S.; Osawa, M. (2002) Electroless deposition of gold thin films on silicon for surface-enhanced infrared spectroelectrochemistry. *Electrochem. Commun.*, *4*, 973-977.
50. Morhart, T. A.; Unni, B.; Lardner, M. J.; Burgess, I. J. (2017) Electrochemical ATR-SEIRAS Using Low-Cost, Micromachined Si Wafers. *Anal. Chem.*, *89*, 11818-11824.
51. Du, P.; Kokhan, O.; Chapman, K. W.; Chupas, P. J.; Tiede, D. M. (2012) Elucidating the Domain Structure of the Cobalt Oxide Water Splitting Catalyst by X-ray Pair Distribution Function Analysis. *J. Am. Chem. Soc.*, *134*, 11096-11099.
52. Diaz-Morales, O.; Ferrus-Suspedra, D.; Koper, M. T. (2016) The importance of nickel oxyhydroxide deprotonation on its activity towards electrochemical water oxidation. *Chem. Sci.*, *7*, 2639-2645.
53. Klähn, M.; Mathias, G.; Kötting, C.; Nonella, M.; Schlitter, J.; Gerwert, K.; Tavan, P. (2004) IR spectra of phosphate ions in aqueous solution: predictions of a DFT/MM approach compared with observations. *J. Phys. Chem. A*, *108*, 6186-6194.
54. Suzuki, M.; Ishiguro, T.; Kozuka, M.; Nakamoto, K. (1981) Resonance Raman spectra, excitation profiles, and infrared spectra of [N, N'-ethylenebis (salicylideniminato)] cobalt (II) in the solid state. *Inorg. Chem.*, *20*, 1993-1996.
55. Jones, R. D.; Summerville, D. A.; Basolo, F. (1979) Synthetic oxygen carriers related to biological systems. *Chem. Rev.*, *79*, 139-179.
56. Tang, I. N.; Munkelwitz, H. R. (1994) Water activities, densities, and refractive indices of aqueous sulfates and sodium nitrate droplets of atmospheric importance. *J. Geophy. Res. : Atmos.*, *99*, 18801-18808.
57. Gerken, J. B.; McAlpin, J. G.; Chen, J. Y. C.; Rigsby, M. L.; Casey, W. H.; Britt, R. D.; Stahl, S. S. (2011) Electrochemical Water Oxidation with Cobalt-Based Electrocatalysts from pH 0–14: The Thermodynamic Basis for Catalyst Structure, Stability, and Activity. *J. Am. Chem. Soc.*, *133*, 14431-14442.
58. Ronald Fawcett, W.; Ryan, P. J. (2010) Is perchlorate ion contact adsorbed from aqueous solutions at polarizable electrodes? *J. Electroanal. Chem.*, *649*, 48-52.
59. Ding, C.; Zhou, X.; Shi, J.; Yan, P.; Wang, Z.; Liu, G.; Li, C. (2015) Abnormal Effects of Cations (Li^+, Na^+, and K^+) on Photoelectrochemical and

Electrocatalytic Water Splitting. *J. Phys. Chem. B*, *119*, 3560-3566.

60. Garcia, A. C.; Touzalin, T.; Nieuwland, C.; Perini, N.; Koper, M. T. M. (2019) Enhancement of Oxygen Evolution Activity of Nickel Oxyhydroxide by Electrolyte Alkali Cations. *Angew. Chem. Int. Ed.*, *58*, 12999-13003.
61. Suntivich, J.; Perry, E. E.; Gasteiger, H. A.; Shao-Horn, Y. (2013) The Influence of the Cation on the Oxygen Reduction and Evolution Activities of Oxide Surfaces in Alkaline Electrolyte. *Electrocata,* , *4*, 49-55.
62. Zaffran, J.; Stevens, M. B.; Trang, C. D. M.; Nagli, M.; Shehadeh, M.; Boettcher, S. W.; Caspary Toroker, M. (2017) Influence of Electrolyte Cations on Ni(Fe)OOH Catalyzed Oxygen Evolution Reaction. *Chem. Mater.*, *29*, 4761-4767.
63. Remsing, R. C.; McKendry, I. G.; Strongin, D. R.; Klein, M. L.; Zdilla, M. J. (2015) Frustrated Solvation Structures Can Enhance Electron Transfer Rates. *J. Phys.Chem. Lett.*, *6*, 4804-4808.
64. Surendranath, Y.; Dincă, M.; Nocera, D. G. (2009) Electrolyte-Dependent Electrosynthesis and Activity of Cobalt-Based Water Oxidation Catalysts. *J. Am. Chem. Soc.*, *131*, 2615-2620.
65. Waegele, M. M.; Gunathunge, C. M.; Li, J.; Li, X. (2019) How cations affect the electric double layer and the rates and selectivity of electrocatalytic processes. *J. Chem. Phys.*, *151*, 160902.
66. Trotochaud, L.; Young, S. L.; Ranney, J. K.; Boettcher, S. W. (2014) Nickel–Iron Oxyhydroxide Oxygen-Evolution Electrocatalysts: The Role of Intentional and Incidental Iron Incorporation. *J. Am. Chem. Soc.*, *136*, 6744-6753.
67. Zhang, Y.; Zhang, H.; Ji, H.; Ma, W.; Chen, C.; Zhao, J. (2016) Pivotal Role and Regulation of Proton Transfer in Water Oxidation on Hematite Photoanodes. *J. Am. Chem. Soc.*, *138*, 2705-2711.
68. Goldsmith, Z. K.; Lam, Y. C.; Soudackov, A. V.; Hammes-Schiffer, S. (2019) Proton Discharge on a Gold Electrode from Triethylammonium in Acetonitrile: Theoretical Modeling of Potential-Dependent Kinetic Isotope Effects. *J. Am. Chem. Soc.*, *141*, 1084-1090.
69. Che, F.; Gray, J. T.; Ha, S.; Kruse, N.; Scott, S. L.; McEwen, J.-S. (2018) Elucidating the Roles of Electric Fields in Catalysis: A Perspective. *ACS Catal.*, *8*, 5153-5174.
70. Chen, L. D.; Urushihara, M.; Chan, K.; Nørskov, J. K. (2016) Electric Field Effects in Electrochemical CO_2 Reduction. *ACS Catal.*, *6*, 7133-7139.
71. Gorin, C. F.; Beh, E. S.; Bui, Q. M.; Dick, G. R.; Kanan, M. W. (2013) Interfacial Electric Field Effects on a Carbene Reaction Catalyzed by Rh Porphyrins. *J. Am. Chem. Soc.*, *135*, 11257-11265.
72. Karlberg, G. S.; Rossmeisl, J.; Nørskov, J. K. (2007) Estimations of electric field effects on the oxygen reduction reaction based on the density functional theory. *Phys. Chem. Chem.Phys.*, *9*, 5158-5161.
73. Ledezma-Yanez, I.; Wallace, W. D. Z.; Sebastián-Pascual, P.; Climent, V.; Feliu, J. M.; Koper, M. T. M. (2017) Interfacial water reorganization as a pH-dependent descriptor of the hydrogen evolution rate on platinum electrodes. *Nat. Energy*, *2*, 17031.
74. Schultz, Z. D.; Shaw, S. K.; Gewirth, A. A. (2005) Potential Dependent Organization of Water at the Electrified Metal−Liquid Interface. J. Am. Chem. Soc., 127, 15916-15922.
75. Toney, M. F.; Howard, J. N.; Richer, J.; Borges, G. L.; Gordon, J. G.; Melroy, O. R.; Wiesler, D. G.; Yee, D.; Sorensen, L. B. (1994) Voltage-dependent ordering of water molecules at an electrode–electrolyte interface. *Nature*, *368*, 444-446.
76. McAlpin, J. G.; Surendranath, Y.; Dincă, M.; Stich, T. A.; Stoian, S. A.; Casey, W. H.; Nocera, D. G.; Britt, R. D. (2010) EPR Evidence for Co(IV) Species Produced During Water Oxidation at Neutral pH. *J. Am. Chem. Soc.*, *132*, 6882-6883.
77. Bajdich, M.; García-Mota, M.; Vojvodic, A.; Nørskov, J. K.; Bell, A. T. (2013) Theoretical Investigation of the Activity of Cobalt Oxides for the Electrochemical Oxidation of Water. *J. Am. Chem. Soc.*, *135*, 13521-13530.
78. Plaisance, C. P.; van Santen, R. A. (2015) Structure Sensitivity of the Oxygen Evolution Reaction Catalyzed by Cobalt(II,III) Oxide. *J. Am. Chem. Soc.*, *137*, 14660-14672.
79. Pham, H. H.; Cheng, M.-J.; Frei, H.; Wang, L.-W. (2016) Surface Proton Hopping and Fast-Kinetics Pathway of Water Oxidation on Co_3O_4 (001) Surface. *ACS Catal.*, *6*, 5610-5617.

Supporting information

Observation of a Potential-Dependent Switch of Water Oxidation Mechanism on Co-Oxide-Based Catalysts

Chaochao Lang[1,3], Jingyi Li[1,3], Ke R. Yang[2,3], Yuanxing Wang[1,3], Da He[1], James E. Thorne[1], Seth Croslow[1], Qi Dong[1], Yanyan Zhao[1], Gabriela Prostko[1], Gary W. Brudvig[2], Victor S. Batista[2*], Matthias M. Waegele[1**], Dunwei Wang[1,4***]

[1]Department of Chemistry, Merkert Chemistry Center, Boston College, 2609 Beacon St., Chestnut Hill, Massachusetts， 02467,United States

[2]Yale Energy Sciences Institute and Department of Chemistry, Yale University, New Haven, Connecticut 06520, United States

[3]These authors contributed equally.

[4]Lead Contact

*Correspondence: victor.batista@yale.edu

**Correspondence: waegele@bc.edu

***Correspondence: dunwei.wang@bc.edu

EXPERIMENTAL PROCEDURES

Materials

$Co(NO_3)_2$ (99.999%, Alfa Aesar), KOH (85%, VWR International), $NaNO_3$ (99.0% min., Alfa Aesar), $NaClO_4$ (99.0% min., Alfa Aesar), KNO_3 (99.0% min., Sigma-Aldrich), K_2HPO_4 (98.0% min., Alf Aesar), KH_2PO_4 (98.0% min., Alf Aesar), Na_2HPO_4 (99.0% min., fisher chemical) and $C_2H_3NaO_2$ (99.0% min., Sigma-Aldrich) were used as received. HF (48 wt.%), $NaAuCl_4 \cdot 2H_2O$ (99.99%; metals basis), Na_2SO_3 (98.5%; for analysis, anhydrous), $Na_2S_2O_3 \cdot 2H_2O$ (99.999%; trace metal basis), NH_4Cl (99.999%; metal basis), and KNO_3 (99.999%, trace metal basis) were used as received from Fisher Scientific. All electrolyte solutions were prepared with deionized water (Barnstead, 18 MΩ-cm resistivity). $H_2{}^{18}O$ (97% enriched) was used as received from Medical Isotopes, NH. D_2O (99.9%) was used as received from Aldrich.

Au Nanofilm Preparation

The gold nanofilm was electrolessly deposited onto Si wafers (IRUBIS GmbH, Germany) following the reported method.[1] The reflective surface of the Si wafer was polished on a mat using 6 and 1 μm diamond slurries (Ted Pella; Redding, CA), then 0.05 μm alumina paste (Electron Microscopy Sciences; Hatfield, PA) with cotton swabs, for 5 min respectively. Then, the Si wafer was cleaned with five consecutive 5 min sonication in ultrapure water and acetone alternately. For the deposition, the Si wafer was first etched in 40% NH_4F for 90 s to remove surface oxide and terminate the surface with hydrogen atoms. Au nanofilm was plated by immersing the Si wafer into a 2:1 mixture of a plating

solution and 2% HF at 60 °C for 120 s. The plating solution contains 15 mM $NaAuCl_4 \cdot 2H_2O$, 150 mM Na_2SO_3, 50 mM $Na_2S_2O_3 \cdot 2H_2O$, and 50 mM NH_4Cl. The resulted resistance of the gold film is 5-10 Ω.

Co-Pi or CoOOH Film Deposition

Co-Pi catalysts were electrodeposited onto substrates in a solution of 0.5 mM $Co(NO_3)_2$ and 0.1 M phosphate buffer (KPi) (pH=7.0) using a Solartron analytical potentiostat by potentiastatical deposition at a potential of 1.14 V vs. the normal hydrogen electrode (NHE) with the passage of 20 mC cm^{-2}.[2] CoOOH electrodes were electrodeposited onto the Pt substrates or Au films in a solution of 10 mM $Co(NO_3)_2$ and 0.1 M $NaCH_3CO_2$ using a VersaStat3 potentiostat (AMETEK; Berwyn, PA). The galvanostatical deposition was set at an anodic current density of 0.05 mA cm^{-2} vs. Pt counter electrode for 5 min.[3]

General Electrochemical Methods

All electrochemical experiments were conducted using a CH Instruments or Solartron analytical potentiostat, a Ag/AgCl reference electrode (0.197 V) or a saturated calomel electrode (SCE, 0.242 V), and a Pt counter electrode. Two types of substrates were used for working electrodes: fluorine-doped tin oxide (FTO) electrode and Pt rotating disk electrode. All the electrochemical measurements were conducted on Co-Pi-coated FTO electrodes in a single cell unless otherwise stated. Rotating disk electrode measurements were conducted using a Pine Instruments MSR rotator and a 5 mm diameter Pt-disk rotating electrode. All electrochemical experiments were performed using a three-electrode electrochemical cell containing a ~15 mL electrolyte solution. Unless otherwise stated, all experiments were performed at ambient temperature and electrode potentials were converted to the reversible hydrogen electrode (RHE) scale using an equation: $E(\text{RHE}) = E(\text{RE}) + E^{o}(\text{RE}) + 0.059 \times \text{pH}$, E(RHE) and E(RE) are the potential versus RHE and reference electrode, E^{o}(RE) is the potential of reference electrode. The electrolyte resistance between working electrode (WE) and RE was measured by electrochemical impedance spectroscopy (EIS) and the resistance was used for *iR* compensation. $E(\text{RE})_{\text{actual}} = E(\text{RE})_{\text{measured}} - iR$ (i and R are the values of current and solution resistance, respectively).

All the water-in-salt (WiS) electrolyte solutions used in the experiments were freshly prepared before every single test. To make the water-in-salt solutions, we first prepared KPi buffer solutions and then added salts into the KPi buffer solutions. pH of all the solutions was adjusted to 7.0 with a freshly prepared 6 M KOH solution in order to prevent the influence of pH on water oxidation activity. Based on the previous literature,[4] water activities (a_w) in 0 m $NaNO_3$ @ 0.1 M KPi , 2 m $NaNO_3$ @ 0.1 M KPi, 4 m $NaNO_3$ @ 0.1 M KPi, 7 m $NaNO_3$ @ 0.1 M KPi are calculated as 1, 0.94, 0.89, 0.83, respectively.

Details of the Electrochemical Measurements

The data in Figures 3 and 4 were collected under steady-state condition, each set of data were repeated three times with a freshly prepared catalyst of similar activity. During the data collection process, the steady-state measurement was performed for about 5 minutes until the current was stable, and then the data was processed by making an average of the last 20 raw data points in steady-state current density vs. potential (j-E) plots (Figure S6 is a representative example of data collection). The data in Figures S7 and S9-S16 were collected under steady-state condition for 3 to 5 min depending on the experiment. The data was processed by making an average of the last 20 raw data points. For Figures S17 and S20, the samples were subjected to 3 consecutive CV measurements. The second and third CV cycles show consistent result, so the third CV cycles were shown. For Figure S19: The data was collected with the same catalyst; we first measured the cyclic voltammetry (CV) plot in D_2O at a scan rate of 20 mV s^{-1} and then performed the same measurement in H_2O.

SEIRAS-ATR Measurement

All in-situ surface-enhanced infrared absorption spectroscopy in attenuated total reflection mode (SEIRAS-ATR) measurements were carried out using nitrogen-purged Bruker Vertex 70 FTIR spectrometer (Billerica, MA) equipped with a liquid-nitrogen-cooled MCT detector (FTIR-16; Infrared Associates; Stuart, FL). The catalyst coated Si wafer was assembled into a customized polyether ether ketone (PEEK) spectroelectrochemical cell, and coupled vertically with an ATR accessory (VeeMax III; Pike Technologies; Madison, WI). All experiments were run with an incident angle of 50°, a resolution of 4 cm^{-1}, and a scanner velocity of 40 kHz. For all spectra shown, change in optical density was calculated according to Absorbance = -log(*S*/*R*), with *S* and *R* referring to the single beam sample spectrum and single beam reference spectrum, respectively.

Simultaneously with the infrared measurement, the CoOOH electrode was subjected to 120 s chronoamperometry from 1.61 to 2.21 V vs. RHE in 0.1 V steps connected with linear sweep voltammetry at a rate of 20 mV s^{-1}. A leakless Ag/AgCl (ET072-1; eDAQ, Colorado Springs, CO) and Pt wire (99.95%; BASi Inc.; West Lafayette, IN) were used as reference electrode and counter electrode, respectively. The electrolyte was prepared with 0.1 M KPi in D_2O, H_2O, or $H_2{}^{18}O$ at pH = 7, and the solution pD value was corrected with a factor of 0.4 from the reading of a pH meter.[5]

Faraday Efficiency Measurement

Faradaic efficiency (FE) was measured with gas chromatography-online method (GCMS-QP2010, Shimadzu). A piece of FTO (1×3 cm^2) was used for growing Co-Pi catalyst. The method for growing the catalyst is the same as that described in the Co-Pi or CoOOH Film Deposition part. O_2 gas was detected. During the experiment, the Co-Pi-coated FTO electrode was immersed into a reaction cell containing about 20 mL 0.1 M KPi neutral electrolyte. A constant current (3 mA) was applied to the electrode in order to generate O_2 bubbles. Then, the O_2 gas was further purged into the gas line of gas chromatography–mass spectrometry (GC-MS) for FE measurement. The equation for calculating FE is given below:

$$FE = \frac{4 \times Oxygen\ amount\ (umol \cdot s^{-1})}{Charge\ (umol \cdot s^{-1})} \times 100\%$$

Computational Details

All DFT calculations were performed with Gaussian 16 Revision C01 software package.[6] We used the B3LYP functional[7,8] in conjugation with the def2-SV(P) basis set[9] for all atoms in the geometry optimization. Frequency analysis was performed to verify the nature of obtained stationary points and obtain harmonic frequencies to calculate the zero-point energies and thermal correction to the entropy and free energy. We used the def2-TZVP basis set[9] for single-point energy calculation to final composite free energy changes. The solvation effect was considered the SMD implicit solvation model[10] and the dispersion correction was considered using Grimme's empirical dispersion correction version 3 with Becke-Johnson damping.[11] We performed geometry optimization in both gas phase and dielectric continuum with SMD. We found that the geometry relaxation in the solvation is quite significant (Figure S22), therefore, all the geometries except H_2 and O_2 used in the manuscript were optimized with the SMD implicit solvation model.

We considered different sizes of Co clusters and found the planar $Co_7O_{24}H_{27}$ cluster with edge-sharing CoO_6 octahedral is the most stable structure, which is consistent with the structure model suggested by EXAFS study.[12] We considered different protonation state of the $Co_7O_{24}H_{27}$ cluster by placing protons at different O positions and found the most stable

configuration corresponds to protonated μ_2-O and μ_3-O bridges, which was used for our mechanistic investigation. We simulated the O-O vibrational frequency of the O-O bond in possible intermediates. We used the atomic masses of specified isotopes and diagonal the Hessian matrix in the mass-weighted coordinates to obtain the vibrational frequency for different isotopes.

The free energy changes of proton-coupled electron transfer steps were calculated with Nørskov's computational hydrogen electrode (CHE) approach[13] to get the free energy change with respect to the reversible hydrogen electrode (RHE) to avoid the explicit use of the hydrated proton and to include the pH effect naturally. Its procedure is given below:

1. Calculate the free energy change (ΔG_1) with respect to the release of ½ equivalence of H_2(g):

$$RH \rightarrow Ox + \frac{1}{2}H_2(g), \Delta G_1$$

2. Use the definition of RHE:

$$\frac{1}{2}H_2(g) \rightarrow H^+(aq) + e^-, \Delta G_2$$

3. Free energy change of a proton-coupled electron transfer step (ΔG_3) with respect to RHE can be calculated by adding ΔG_1 and ΔG_2:

$$RH \rightarrow Ox + H^+ + e^-, \Delta G_3 = \Delta G_1 + \Delta G_2$$

We also considered the water oxidation mechanisms on CoOOH. Given the nature of this system, we applied periodic boundary condition to study the catalytic mechanism on CoOOH surfaces. All calculations for the CoOOH system were performed with the Vienna Ab initio Simulation Package (VASP).[14,15,16,17] We use the Perdew-Burke-Ernzerhof (PBE) exchange-correlation functional[18] in conjugation with the projected-augmented wave (PAW) method[19,20] to describe the ion-electrons interactions. A cutoff energy of 500 eV was chosen for the plane wave basis set in all calculations. We used the Gaussian smearing method to accelerate SCF convergence and the σ value was chosen to be 0.1 eV. The standard GGAs fail for strongly correlated systems such as the d electrons of Co. All calculations involving Ir and Ce atoms were performed with the spin-polarized DFT+*U* method, using the rotational-invariant formalism developed by Dudarev et al.[21] The empirical U_{eff} parameters were chosen to be 3.4 eV for Co 3d electrons.[22]

A 9 × 9 × 9 Monckhorst-Pack type k-point grid[23] was chosen for the optimization of bulk ceria. The energy convergence criterion was set to be 10^{-6} eV per unit cell and the geometry convergence criterion was set to be 10^{-5} eV per unit cell for energy difference between two consecutive ionic steps. The optimized lattice constants $a = b = 2.88$ Å and $c = 13.17$ Å are in good agreement with experimental lattice constant of $a = b = 2.85$ Å and $c = 13.15$ Å.[24]

We prepared slab models for the CoOOH (012) surface to study the water oxidation mechanisms on the the CoOOH (012) surface. CoOOH (012) surface with 3 layers of Co atoms with both sides terminated by water ligands are used in the study (Figure S21). A vacuum layer of ~ 15 Å was used to minimize the artificial interactions between periodic images. A supercell of 13.52 Å × 31.54 Å × 14.37 Å was used to model the CoOOH (012) surface. The atoms in the bottom one layers were fixed at their optimized positions, while the atoms in the top two layers, as well as the adsorbates, were allowed to relax during geometry optimization. A 1 × 1 × 1 Monckhorst-Pack type k-point grid was used for all surface structure relaxations unless otherwise noted. The energy convergence criterion was set to be 10^{-5} eV per super cell and the force convergence criterion of 0.03 eV $Å^{-1}$.

The calculations of isolated small molecules were performed with a supercell of 15.0 Å × 15.0 Å × 15.0 Å. The Gaussian smearing method and a σ value of 0.1 eV were used in the calculations. A 1 × 1 × 1 Monckhorst-Pack type k-point grid was used to sample the Brillouin zone and the SCF convergence criterion was set to be 10^{-5} eV per unit cell.

The energy changes obtained from the periodic boundary calculations were corrected by the thermo-correction from the cluster model to obtain the free energy changes given in Figure S27. The saturated vapor pressure of water at 298.15 K (3.169 kPa) was used to obtain the free energy changes of $H_2O(g) \rightarrow H_2O(l)$.

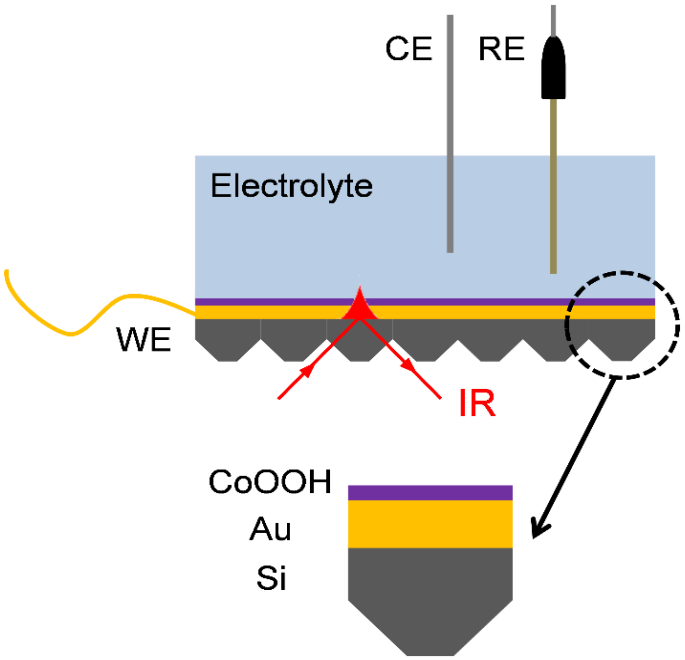

Figure S1. The experimental configuration is schematically illustrated. The key enabling factor is the Si ATR substrate with gratings for directly probing the surface species. WE, CE, and RE denote the working electrode, counter electrode, and reference electrode, respectively.

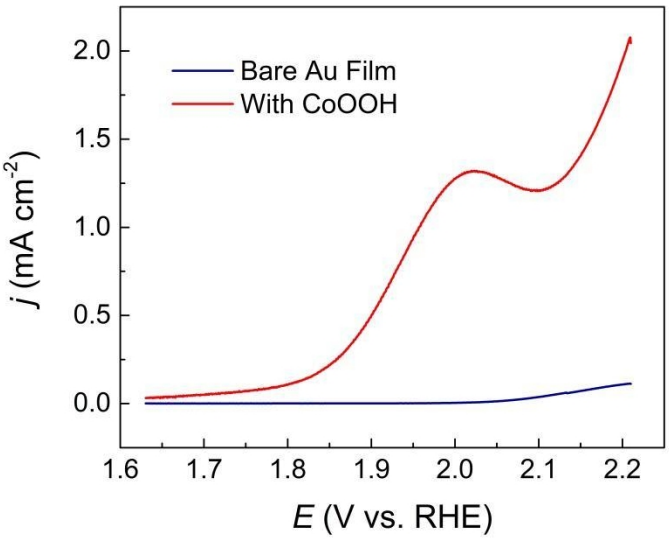

Figure S2. Water oxidation activity comparison between bare Au film and CoOOH-Au sample. The CVs were collected from 1.61 to 2.21 V at a scan rate of 20 mV s^{-1}. The current data are from the third forward scan of the catalyst. All the data were corrected with *iR* compensation.

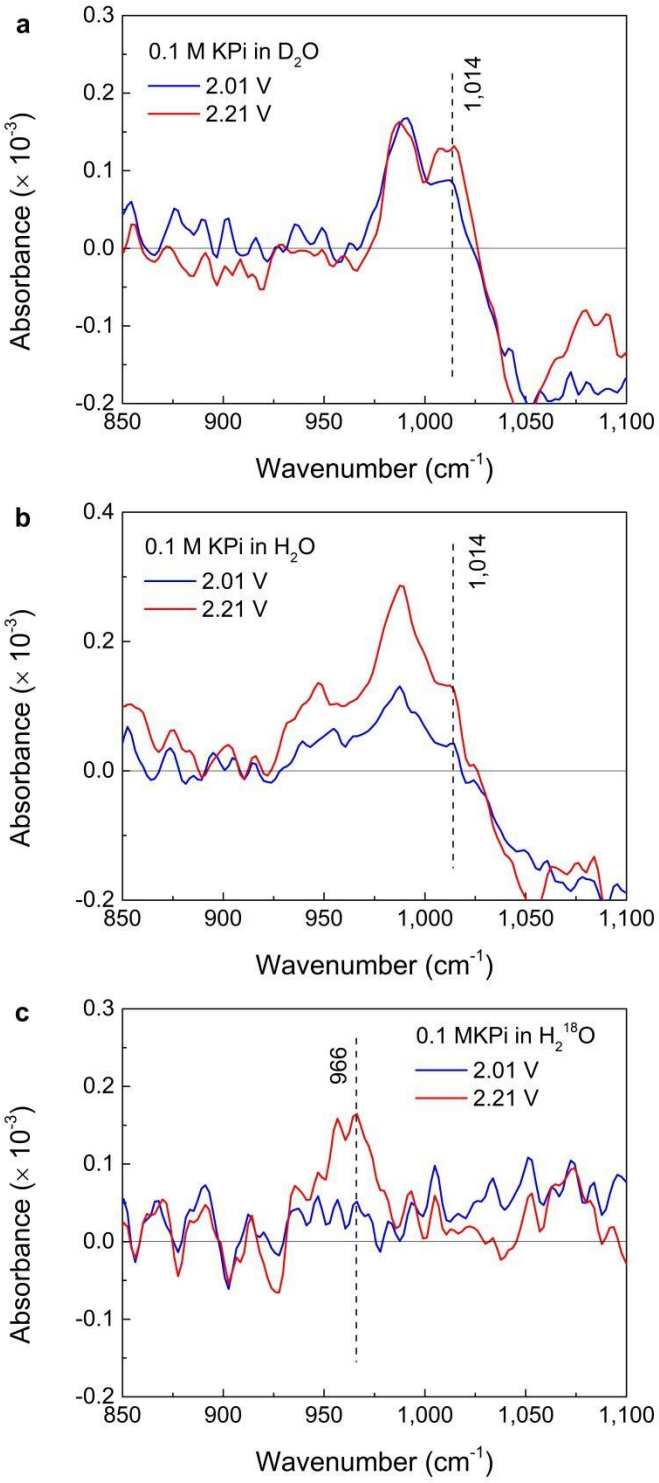

Figure S3. The intensity of the band centered at 1,014 cm^{-1} at 2.21 V increases with increasing applied potential in 0.1 M KPi with (**a**) D_2O, (**b**) H_2O, and (**c**) $H_2{}^{18}O$.

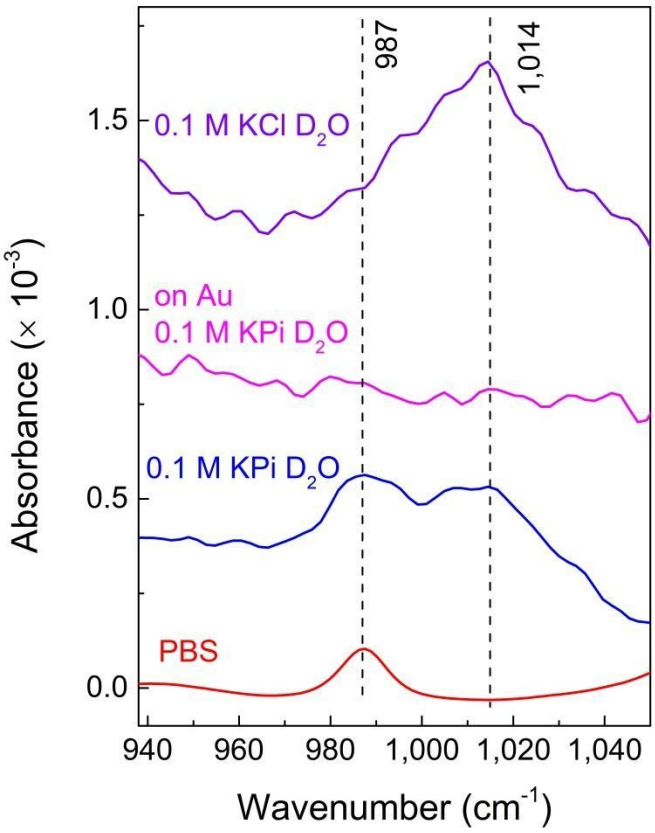

Figure S4. A control experiment for ruling out the complication brought up by solution species: A prominent band at 1,014 cm^{-1} is observable in 0.1 M KCl at 2.21 V (purple), while the band does not show up on a bare Au control sample at same potential (pink).

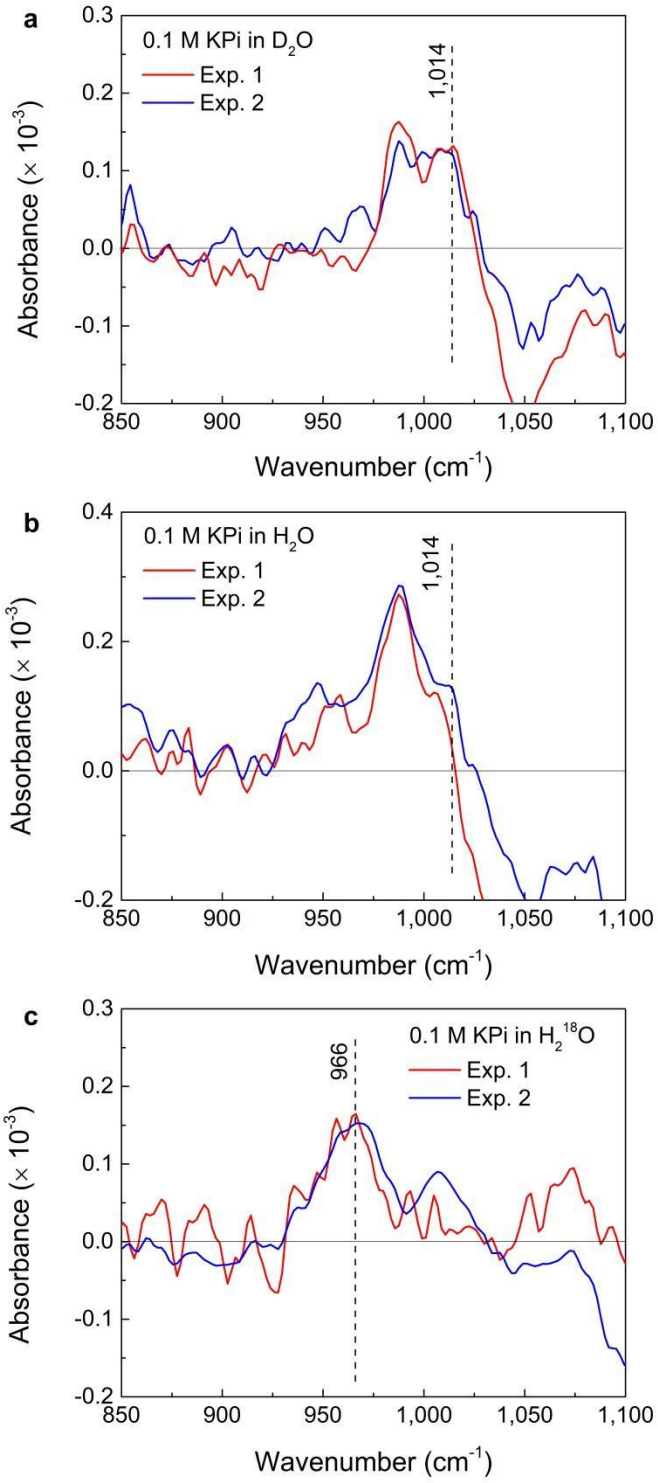

Figure S5. SEIRAS data collected on different samples in 0.1 M KPi with (**a**) D_2O, (**b**) H_2O, and (**c**) $H_2{}^{18}O$, to demonstrate reproducibility at 2.21 V. Reference spectra were taken at 1.61 V.

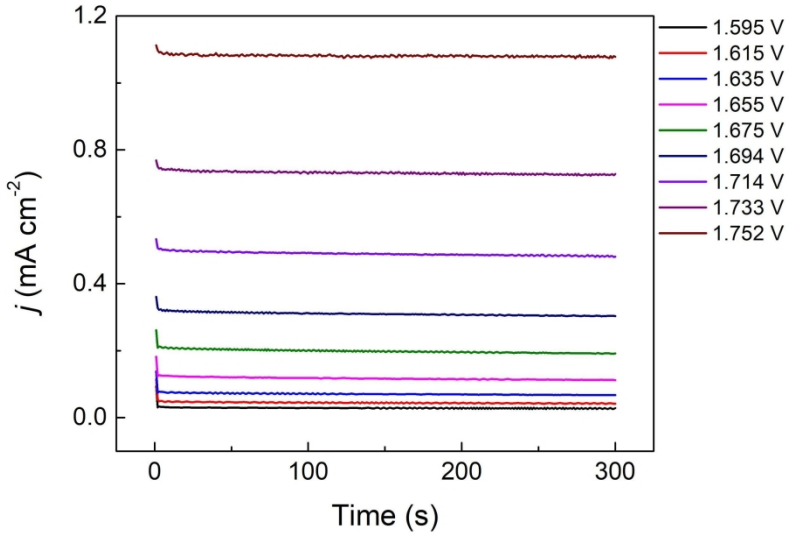

Figure S6. Representative steady-state electrochemical *j-t* plots of water oxidation on Co-Pi catalysts in 0.1 M KPi containing 2 m $NaNO_3$ electrolyte (a_w= 0.94) at various potentials as indicated. The electrode potential was corrected for the *iR* drop.

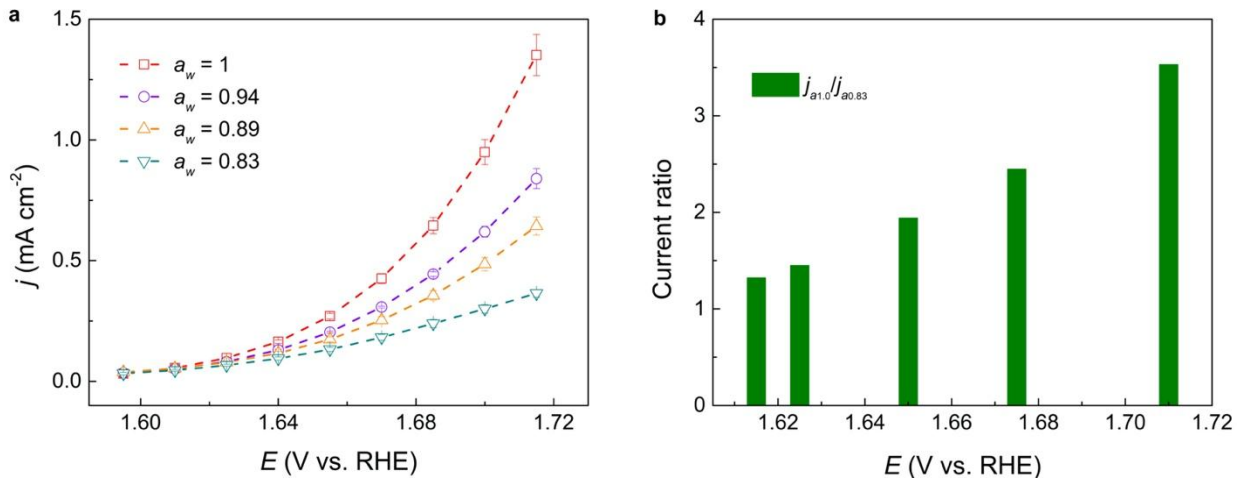

Figure S7. Steady-state water oxidation current density as in **Figures 3** and **4**, but collected on a CoOOH-coated Pt electrode under stirring condition. The data were derived from an average of three independent experiments for each a_w. Error bars denote the standard deviation of three individual measurements. The electrode potential was corrected for the *iR* drop.

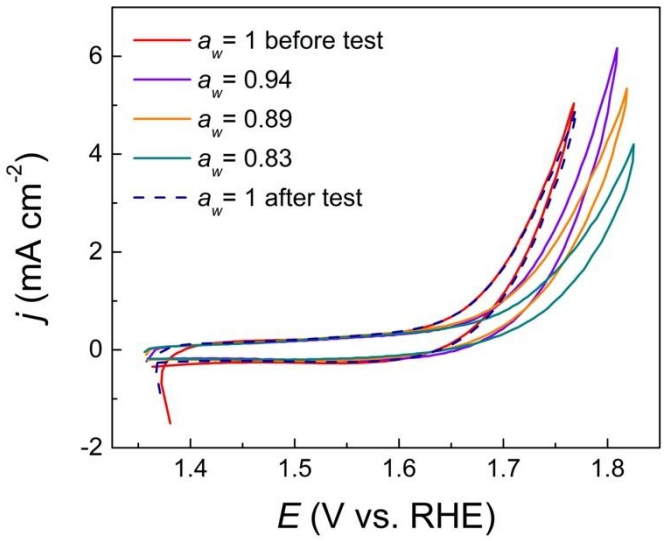

Figure S8. CV stability test of the same Co-Pi catalyst before and after a series of CVs in water-in-salt electrolytes at a scan rate of 20 mV s^{-1}. The CV measurements are from the first cycle of the catalyst. The electrode potential was corrected for the *iR* drop.

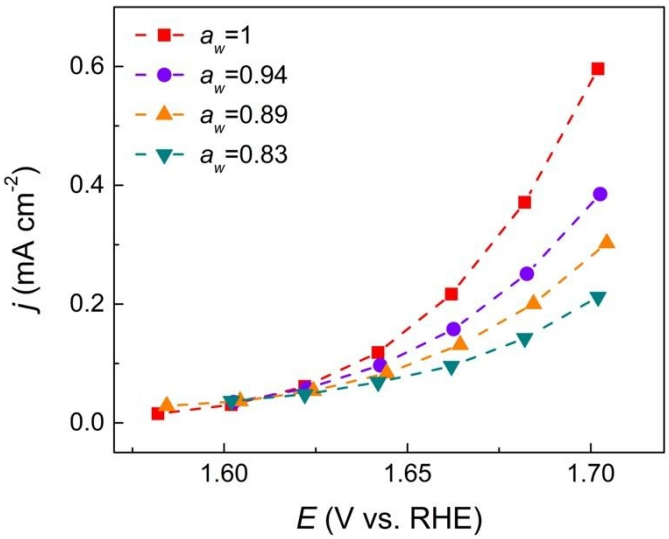

Figure S9. Steady-state water oxidation current density as in **Figure 3**, but collected on a Co-Pi-coated Pt RDE at a rotation rate of 2,000 rpm. The electrode potential was corrected for the *iR* drop.

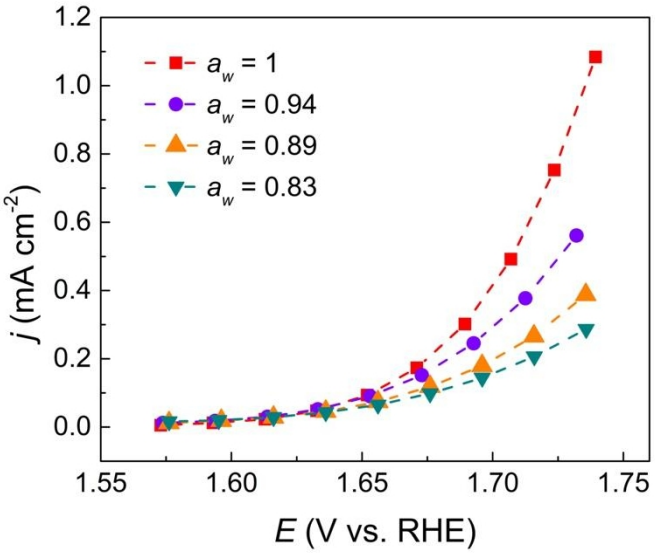

Figure S10. Steady-state water oxidation current density on a Co-Pi-coated Pt RDE as that in **Figure S9** but collected at a rotation rate of 0 rpm. The electrode potential was corrected for the *iR* drop.

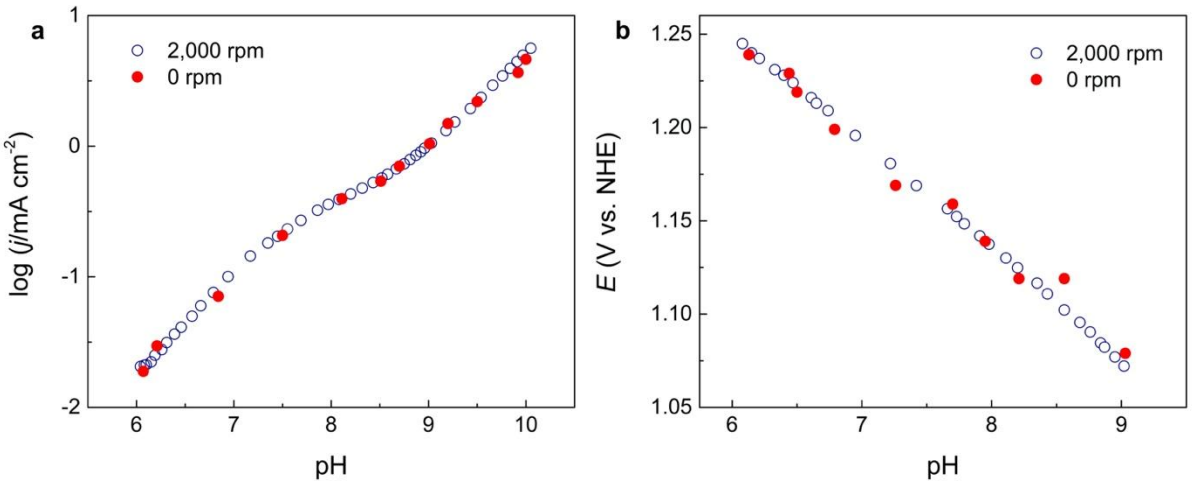

Figure S11. pH titration under (**a**) controlled-potential (1.237 V vs. NHE) and (**b**) controlled-current (30 μA cm^{-2}) for a Co-Pi-coated Pt RDE in 2 m $NaNO_3$@0.1 M KPi (a_w= 0.94) at two different rotation rates, as indicated. These data were collected under steady state conditions.

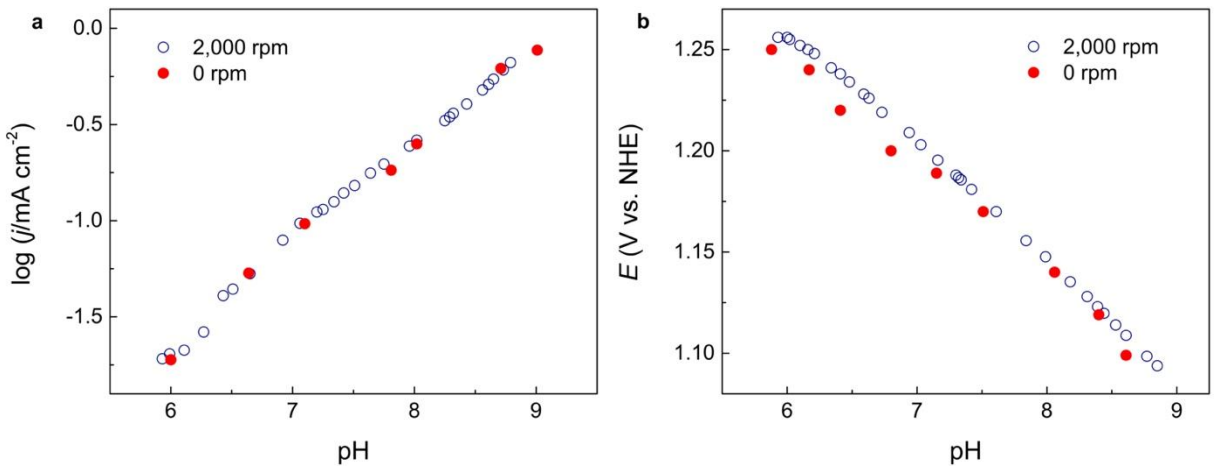

Figure S12. pH titration under (**a**) controlled-potential (1.237 V vs. NHE) and (**b**) controlled-current (30 μA cm^{-2}) for a Co-Pi-coated Pt RDE in 4 m $NaNO_3$@0.1 M KPi (a_w= 0.89) at two different rotation rates, as indicated. These data were collected under steady state conditions.

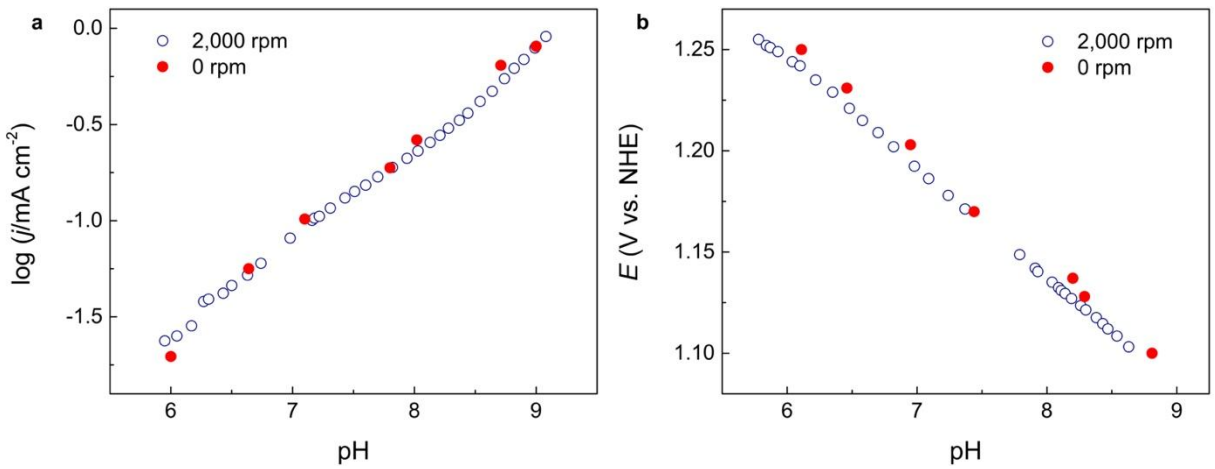

Figure S13. pH titration under (**a**) controlled-potential (1.237 V vs. NHE) and (**b**) controlled-current (30 μA cm^{-2}) for a Co-Pi-coated Pt RDE in 7 m $NaNO_3$@0.1 M KPi (a_w= 0.83) at two different rotation rates, as indicated. These data were collected under steady state conditions.

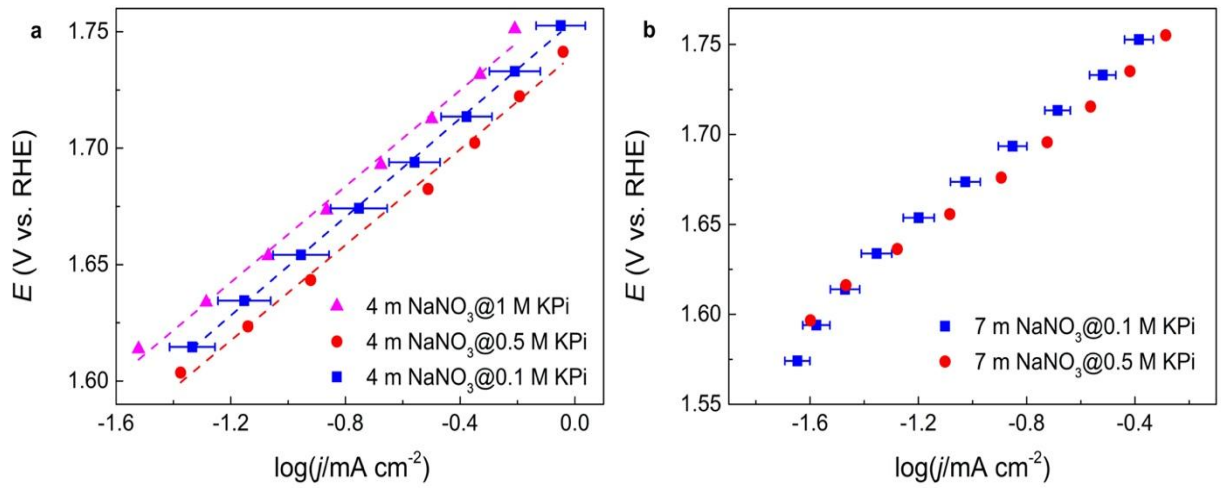

Figure S14. Tafel data for (**a**) 4 m $NaNO_3$ (**b**) 7 m $NaNO_3$ containing different concentrations of KPi indicate that there is no significant dependence of the slope and reaction rate on KPi concentration. These data were collected under steady state conditions. The electrode potential was corrected for the *iR* drop. Error bars denote the standard deviation of three independent measurements.

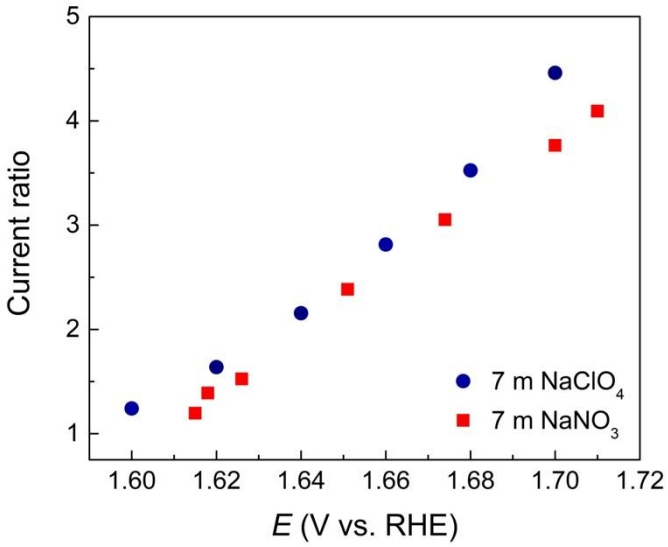

Figure S15. To study the influence of the anion on the electrocatalytic activity, we replaced $NaNO_3$ with $NaClO_4$ to perform a similar potentiostatic measurement. The buffer solution was 0.1 M NaPi to avoid precipitation of $KClO_4$. These data were collected under steady state 0.2 M conditions. The electrode potential was corrected for the *iR* drop.

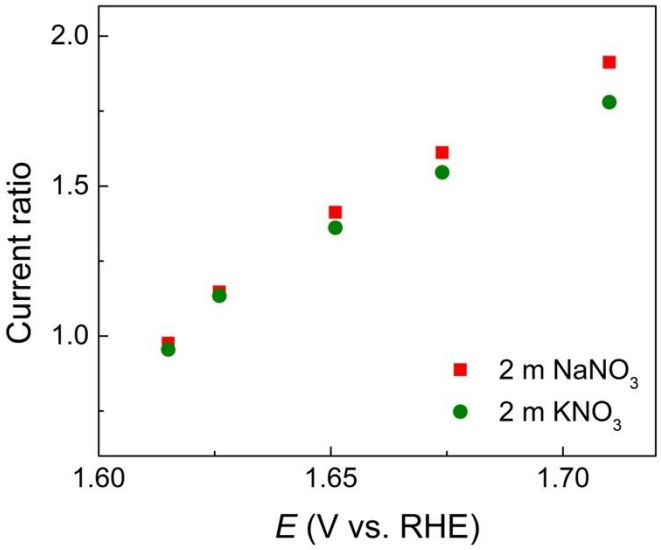

Figure S16. Current modulation ratios in a_w = 0.94 with different cations. The concentration is limited by the KNO_3 solubility. These data were collected under steady-state conditions. The electrode potential was corrected for the *iR* drop.

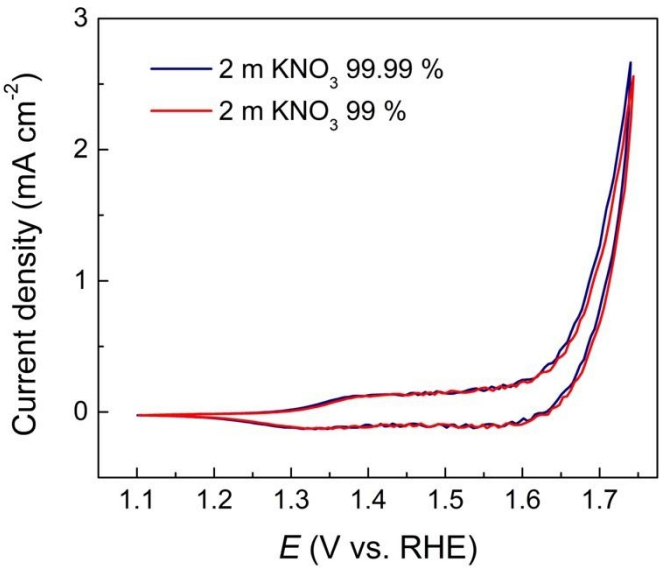

Figure S17. Comparison of CV data collected in 2 m 99% KNO_3 and 2 m 99.99% KNO_3, at a scan rate of 20 mV s^{-1}. The CV measurements are from the third cycle of the catalyst. The electrode potential was corrected for the *iR* drop.

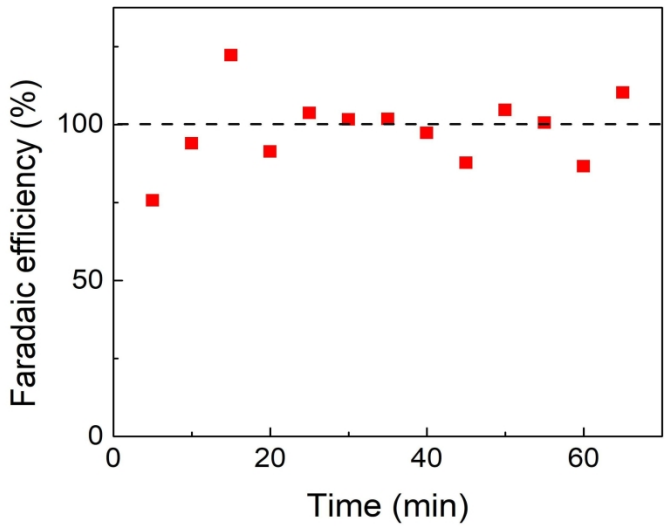

Figure S18. The Faradaic efficiency for O_2 was measured at a current of 3 mA in 7 m $NaNO_3$ solution containing 0.1 M KPi buffer with gas chromatography.

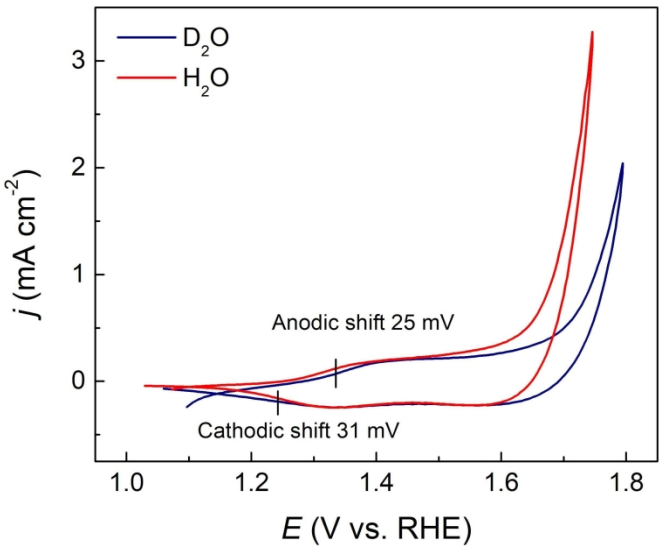

Figure S19. Comparison of CV data collected in D_2O and H_2O, at a scan rate of 20 mV s^{-1}. The electrode potential was corrected for the *iR* drop. The CV measurements are from the first cycle of the catalyst. The shift of the half-wave potential was calculated according to the following equation:

$$Shift\ of\ redox\ half\ wave\ potential = \frac{Shift\ of\ anodic\ feature + Shift\ of\ cathodic\ feature}{2}$$

$$= \frac{25\ mV + \ 31\ mV}{2} = 28\ mV$$

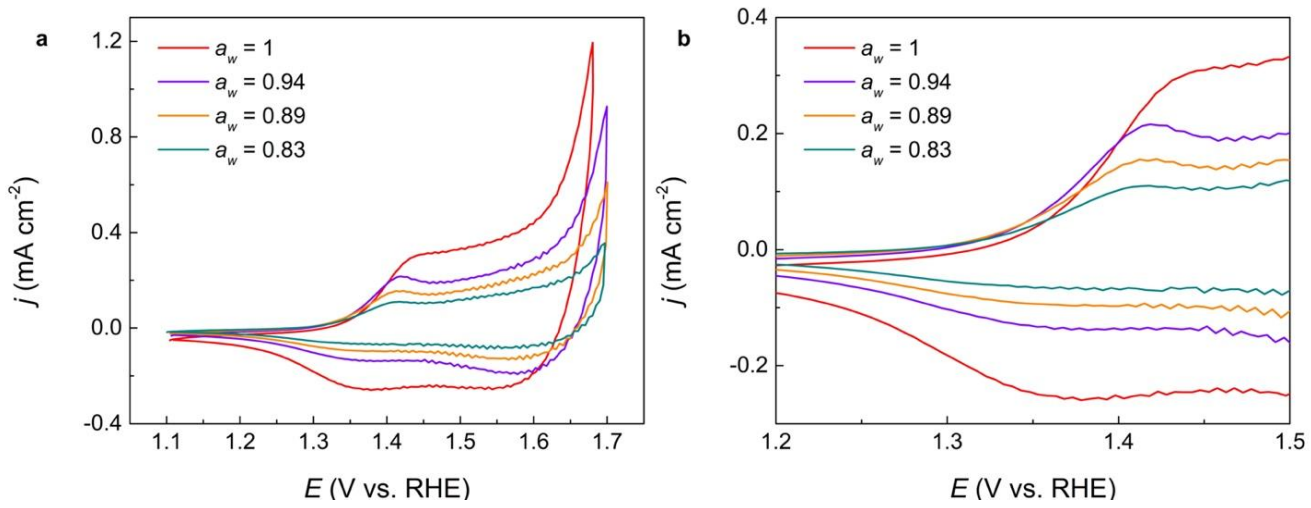

Figure S20. A series of CVs of the Co-Pi catalyst in water-in-salt electrolytes at a scan rate of 20 mV s^{-1} in (**a**) full range and (**b**) zoomed range. The CV measurements are from the third cycle of the catalyst. The electrode potential was corrected for the *iR* drop.

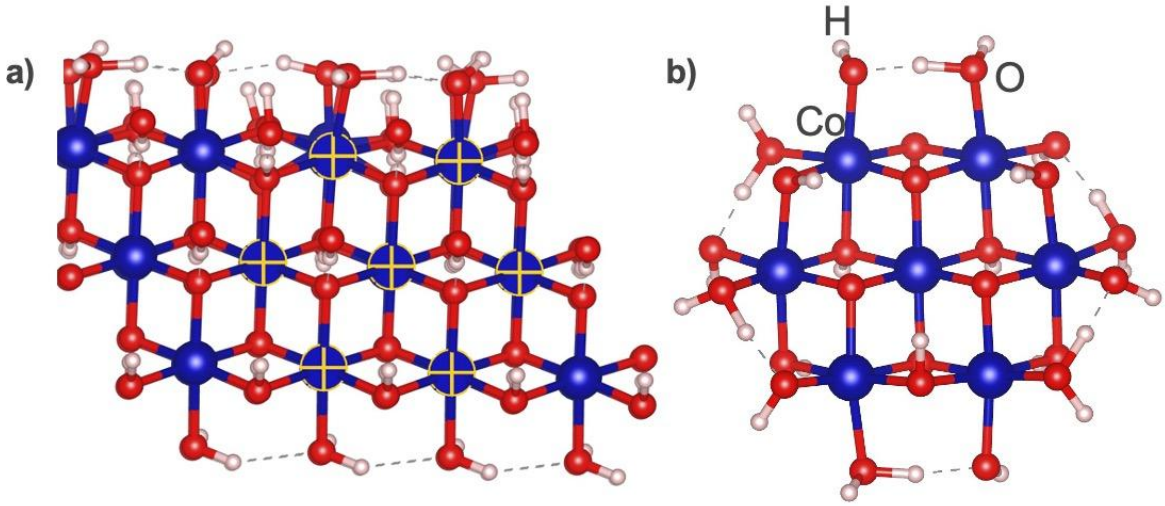

Figure S21. The structural models of (**a**) the CoOOH (012) surface and (**b**) the Co-Pi catalyst. The cluster model of the Co-Pi catalyst is based on previous EXAFS study.[12] The Co7 core in the cluster model resemble the highlighted Co7 unit in the CoOOH structure. The atomic model of Co cluster ($Co_7O_{24}H_{27}$) is constructed for our theoretical study with the water and hydroxides ligands. The blue, red, and white spheres represent Co, O, and H atoms, respectively.

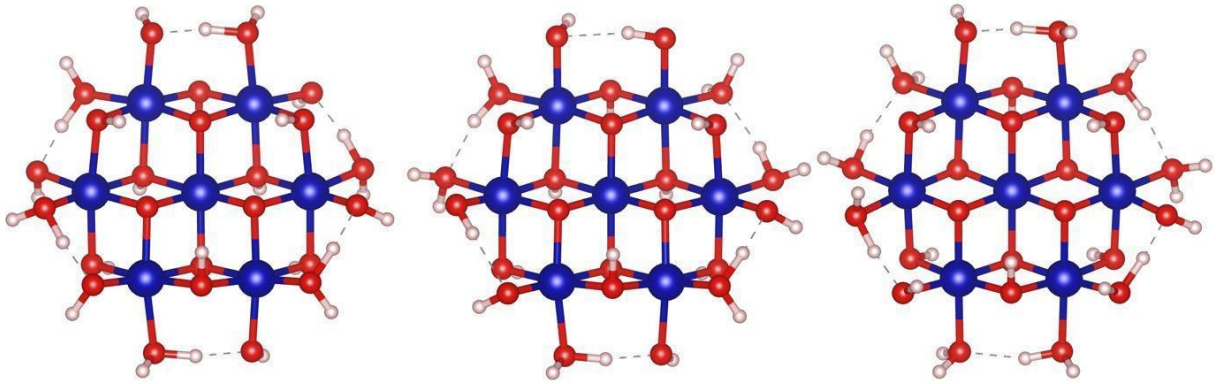

Figure S22. Relative free energies of the $Co_7O_{24}H_{27}$ cluster with different protonation states in gas phase and in aqueous solution. The most stable protonation state (left) has alternative HO---H_2O hydrogen bond interactions at peripheric Co pairs and the bottom μ_3-O bridges being protonated. Destroying the alternative HO---H_2O hydrogen bond interaction by preparing H_2O---H_2O and HO---HO hydrogen bonding pattern increases the energy (middle). Removing the protons from μ_3-O bridges to terminal OH^- increases the energy (right) since it disturbs the strong HO---H_2O hydrogen bond interactions. We choose the most stable protonation state (left) for our mechanistic study. It is worth pointing out that the free energy different in the solution is much smaller than in the gas phase due to a large geometry relaxation due to the high dielectric solvation environment. Therefore, we optimized all geometries in the SMD implicit solvation model.

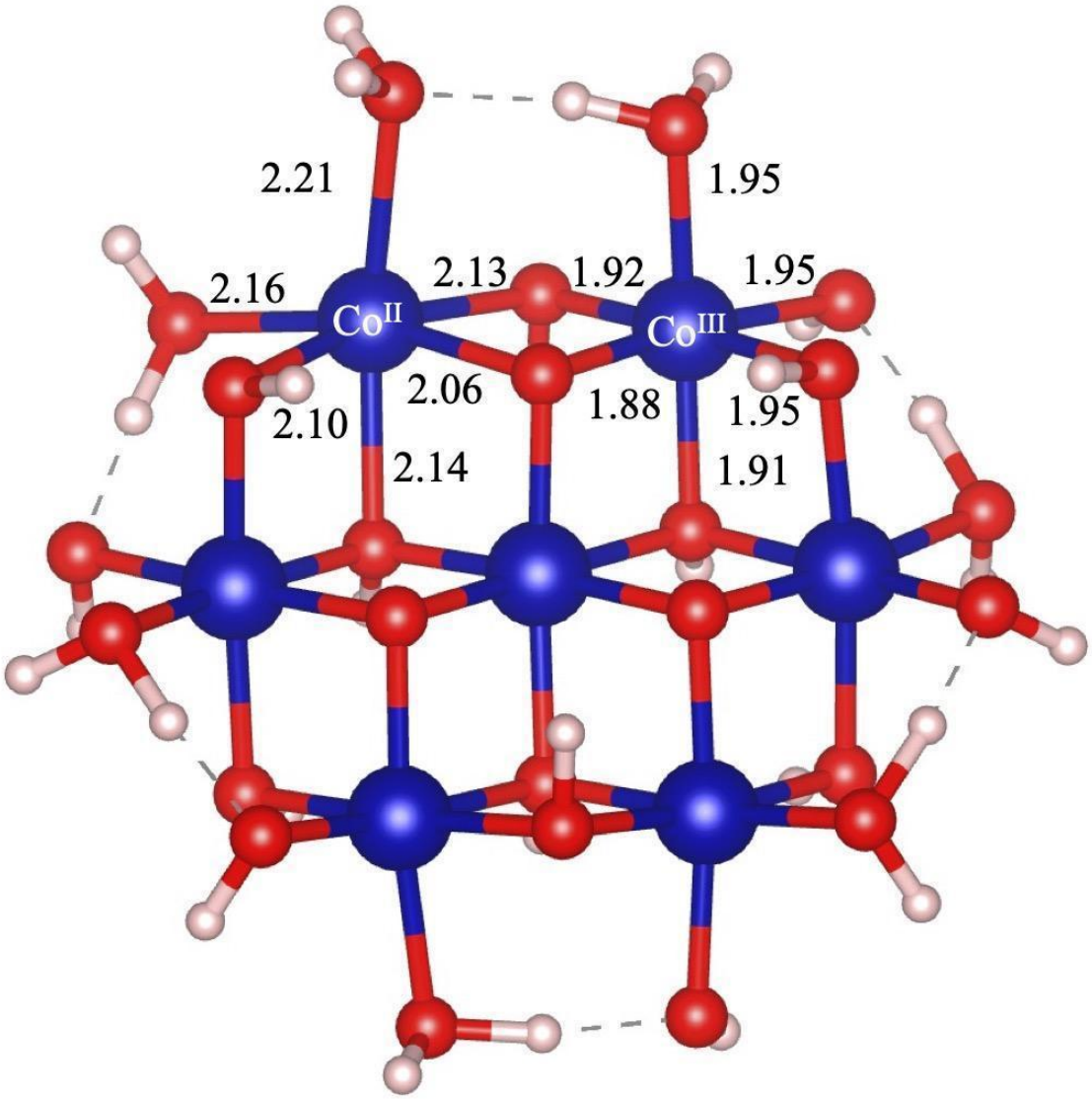

Figure S23. Optimized Co–O bond lengths around the Co(II) and Co(III) centers in intermediate **I**. The Co–O bond lengths are somewhat longer around the Co(II) center since the ground state of Co(II) is a high-spin quartet. In contrast, the low-spin Co(III) center has much shorter Co–O bond lengths and stronger metal-ligand interactions which are crucial for the stability of the molecular-like Co-Pi water oxidation catalyst.

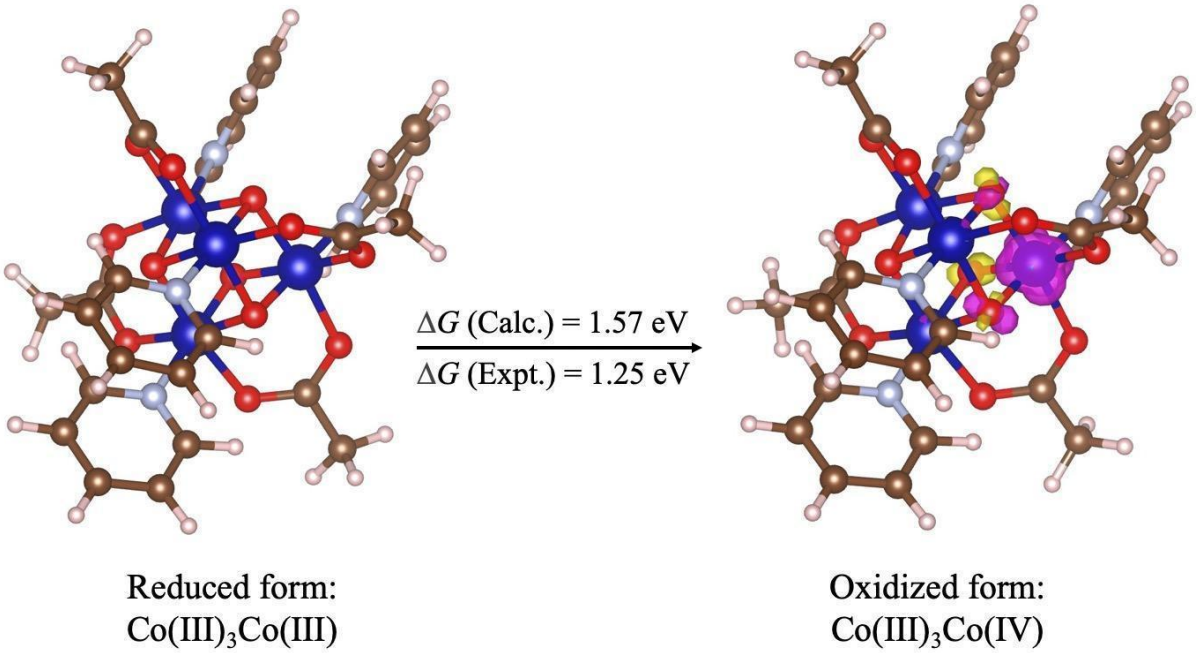

Figure S24. Optimized structures of the $Co_4O_4(OAc)_4(Py)_4$ complex in its reduced and oxidized form. Magenta and yellow isosurfaces show the alpha and beta spin density distribution and are plotted with an isovalue of 0.01 $Å^{-3}$. The calculated and experimental[25] free energy changes with respect to the normal hydrogen electrode (NHE) are 1.57 and 1.25 eV, respectively. Our calculation using the B3LYP functional overestimates the potential for oxidation potential of Co(III) to Co(IV) by 0.3 eV, which is consistent with a recent benchmark study,[26] highlighting the difficulty to describe the high oxidation Co complex.

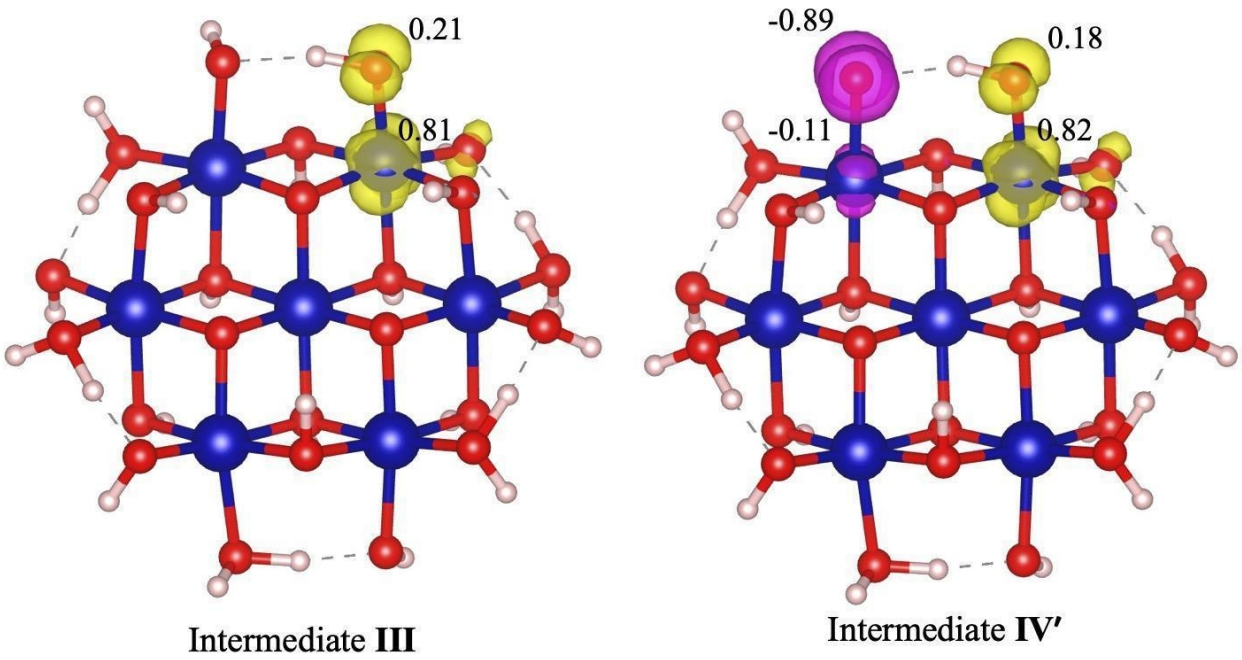

Figure S25. Optimized structures of intermediates **III** and **IV′**. Magenta and yellow isosurfaces show the alpha and beta spin density distribution and are plotted with an isovalue of 0.01 $Å^{-3}$. The numbers next to Co and O ions indicate their Mulliken spin density population. It can be seen clearly that the OH^- coordinated to the Co(IV) center has significant radical character while the Co(IV)=O in intermediate **IV′** is best described as Co(III)–O•.

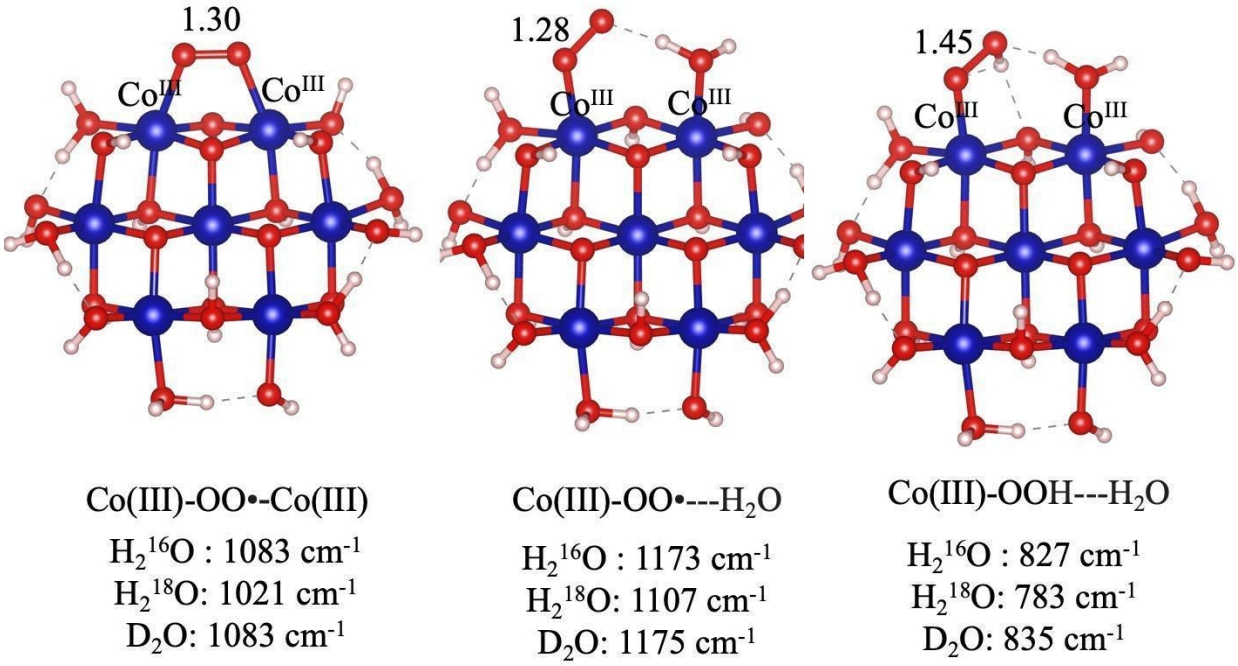

Figure S26. Calculated O–O vibrational frequencies and associated isotope shifts for possible intermediates.

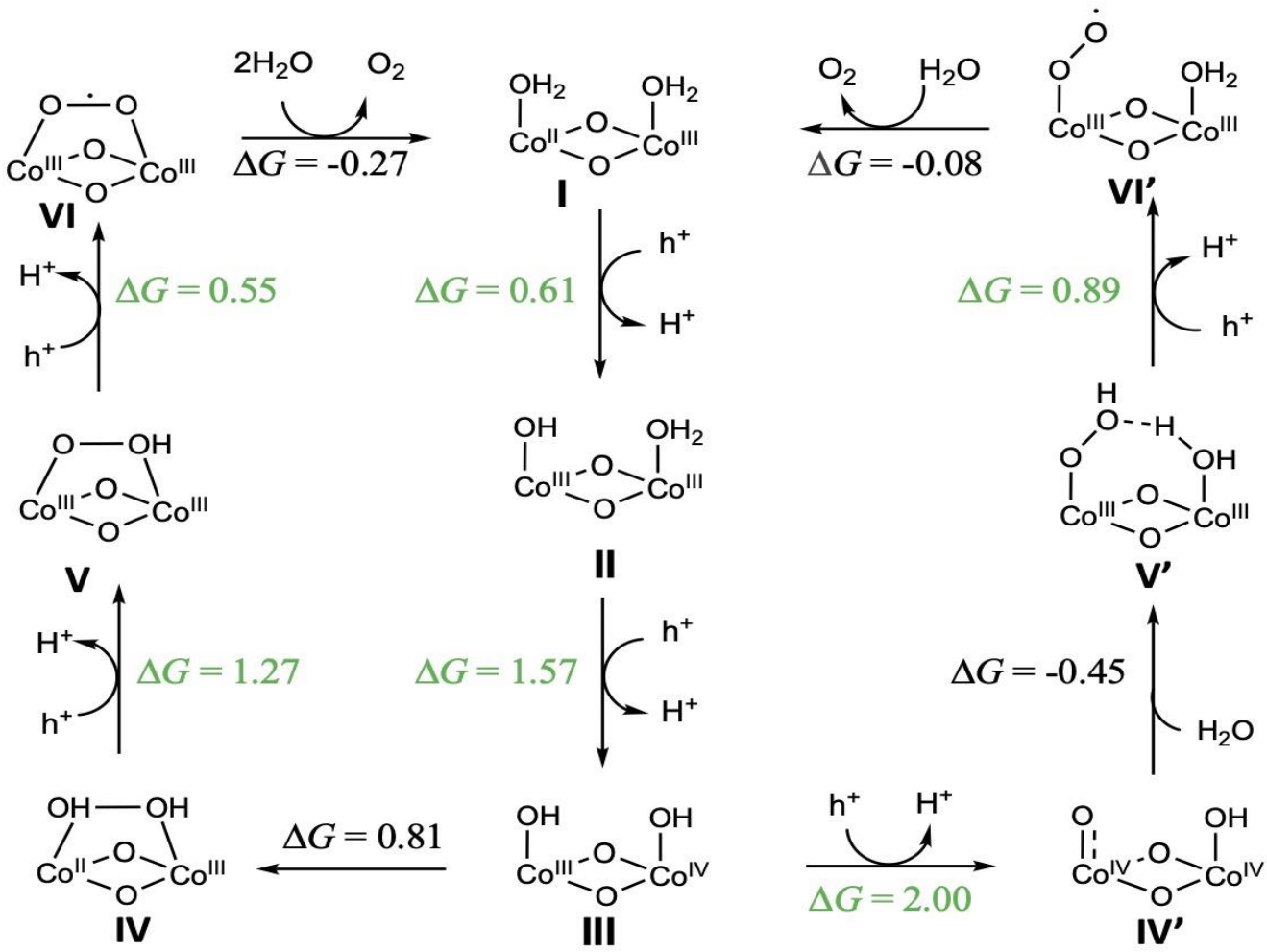

Figure S27. Possible routes of water oxidation on the CoOOH (012) surface suggested by the DFT calculations. Similar to the results of Co-cluster model for Co-Pi system, the IMOC mechanism is possible under low applied potential while the WNA mechanism require higher potential to be accessible. The calculated free energy changes (ΔG) are given in the unit of eV. The numbers shown in green are the free energy changes of electrochemical steps vs. the computed hydrogen electrode.

Table S1. Viscosities (η), densities (d), and stagnant layer thickness (y_s) of water-in-salt electrolytes.

m (mol/kg)	η (cP)	d (g/mL)	y_s at f =2000 rpm (μm)
0[a]	1	1	249
2.14[b]	1.04	1.11	241
3.32[b]	1.19	1.16	252
4.62[b]	1.30	1.21	258
6.02[b]	1.62	1.26	283
7.56[b]	1.92	1.30	302

[a] Based on the assumption that the viscosity and density of 0 m solution are 1 cP and 1g/mL.
[b] Based on Ref (27)

The stagnant layer thickness (y_s) is calculated based on

$$y_s = 3.6 \times \left(\frac{\upsilon}{\omega}\right)^{\frac{1}{2}}$$

where $\upsilon = \frac{\eta}{d}$ is the kinematic viscosity, and $\omega = \frac{2\pi f}{60}$ is the angular rotation rate at f (rotation rate in revolutions per minute).[27]

The viscosity of water-in-salt solutions are expected to increase from 1 to ~ 2 cP when increasing the molality from 0 to 7.56 m.[28] The stagnant layer thicknesses at all molalities fall in the range of 200-300 μm, which are expected for conventional RDE measurements at a rotating rate of 2000 rpm. The thickness first decreases with the addition of high molality salt, then it increases as the molality increases. When the molality increases from 2 to 7.56 m, the thickness increases ca. 25%.

References

1. Miyake, H.; Ye, S.; Osawa, M. (2002) Electroless deposition of gold thin films on silicon for surface-enhanced infrared spectroelectrochemistry. *Electrochem. Commun.*, *4*, 973-977.
2. Surendranath, Y.; Kanan, M. W.; Nocera, D. G. (2010) Mechanistic Studies of the Oxygen Evolution Reaction by a Cobalt-Phosphate Catalyst at Neutral pH. *J. Am. Chem. Soc.*, *132*, 16501-16509.
3. Friebel, D.; Bajdich, M.; Yeo, B. S.; Louie, M. W.; Miller, D. J.; Sanchez Casalongue, H.; Mbuga, F.; Weng, T.-C.; Nordlund, D.; Sokaras, D.; Alonso-Mori, R.; Bell, A. T.; Nilsson, A. (2013) On the chemical state of Co oxide electrocatalysts during alkaline water splitting. *Phys. Chem. Chem. Phys.*, *15*, 17460-17467.
4. Tang, I. N.; Munkelwitz, H. R. (1994) Water activities, densities, and refractive indices of aqueous sulfates and sodium nitrate droplets of atmospheric importance. *J. Geophy. Res. : Atmos.*, *99*, 18801-18808.
5. Li, W.; Sheehan, S. W.; He, D.; He, Y.; Yao, X.; Grimm, R. L.; Brudvig, G. W.; Wang, D. (2015) Hematite-Based Solar Water Splitting in Acidic Solutions: Functionalization by Mono- and Multilayers of Iridium Oxygen-Evolution Catalysts. *Angew. Chem. Int. Ed.*, *54*, 11428-11432.
6. Frisch, M. J.; Trucks, G. W.; Schlegel, H. B.; Scuseria, G. E.; Robb, M. A.; Cheeseman, J. R.; Scalmani, G.; Barone, V.; Petersson, G. A.; Nakatsuji, H.; et al.: Gaussian 16 Rev. C.01. Wallingford, CT, 2016.
7. Becke, A. D. (1993) Density-functional thermochemistry. III. The role of exact exchange. *J. Chem. Phys.*, *98*, 5648-5652.
8. Stephens, P. J.; Devlin, F. J.; Chabalowski, C. F.; Frisch, M. J. (1994) Ab initio calculation of vibrational absorption and circular dichroism spectra using density functional force fields. *J. Phys. Chem.*, *98*, 11623-11627.
9. Weigend, F.; Ahlrichs, R. (2005) Balanced basis sets of split valence, triple zeta valence and quadruple zeta valence quality for H to Rn: Design and assessment of accuracy. *Phys. Chem. Chem. Phys.*, *7*, 3297-3305.
10. Marenich, A. V.; Cramer, C. J.; Truhlar, D. G. (2009) Universal Solvation Model Based on Solute Electron Density and on a Continuum Model of the Solvent Defined by the Bulk Dielectric Constant and Atomic Surface Tensions. *J. Phys. Chem. B*, *113*, 6378-6396.
11. Grimme, S.; Ehrlich, S.; Goerigk, L. (2011) Effect of the damping function in dispersion corrected density functional theory. *J. Comput. Chem.*, *32*, 1456-1465.
12. Kanan, M. W.; Yano, J.; Surendranath, Y.; Dincă, M.; Yachandra, V. K.; Nocera, D. G. (2010) Structure and Valency of a Cobalt−Phosphate Water Oxidation Catalyst Determined by in Situ X-ray Spectroscopy. *J. Am. Chem. Soc.*, *132*, 13692-13701.
13. Nørskov, J. K.; Rossmeisl, J.; Logadottir, A.; Lindqvist, L.; Kitchin, J. R.; Bligaard, T.; Jónsson, H. (2004) Origin of the Overpotential for Oxygen Reduction at a Fuel-Cell Cathode. *J. Physi. Chem. B*, *108*, 17886-17892.

14. Kresse, G.; Hafner, J. (1993) Ab initio molecular dynamics for liquid metals. *Phys. Rev. B*, *47*, 558-561.
15. Kresse, G.; Hafner, J. (1994) Ab initio molecular-dynamics simulation of the liquid-metal--amorphous-semiconductor transition in germanium. *Phys. Rev. B*, *49*, 14251-14269.
16. Kresse, G.; Furthmüller, J. (1996) Efficiency of ab-initio total energy calculations for metals and semiconductors using a plane-wave basis set. *Computational Materials Science*, *6*, 15-50.
17. Kresse, G.; Furthmüller, J. (1996) Efficient iterative schemes for ab initio total-energy calculations using a plane-wave basis set. *Phys. Rev. B*, *54*, 11169-11186.
18. Perdew, J. P.; Burke, K.; Ernzerhof, M. (1996) Generalized Gradient Approximation Made Simple. *Phys. Rev. Lett.*, *77*, 3865-3868.
19. Blöchl, P. E. (1994) Projector augmented-wave method. *Phys. Rev. B*, *50*, 17953-17979.
20. Kresse, G.; Joubert, D. (1999) From ultrasoft pseudopotentials to the projector augmented-wave method. *Phys. Rev. B*, *59*, 1758-1775.
21. Dudarev, S. L.; Botton, G. A.; Savrasov, S. Y.; Humphreys, C. J.; Sutton, A. P. (1998) Electron-energy-loss spectra and the structural stability of nickel oxide: An LSDA+U study. *Phys. Rev. B*, *57*, 1505-1509.
22. Jain, A.; Hautier, G.; Ong, S. P.; Moore, C. J.; Fischer, C. C.; Persson, K. A.; Ceder, G. (2011) Formation enthalpies by mixing GGA and GGA $+$ U calculations. *Phys. Rev. B*, *84*, 045115.
23. Monkhorst, H. J.; Pack, J. D. (1976) Special points for Brillouin-zone integrations. *Phys. Rev. B*, *13*, 5188-5192.
24. Delaplane, R. G.; Ibers, J. A.; Ferraro, J. R.; Rush, J. J. (1969) Diffraction and Spectroscopic Studies of the Cobaltic Acid System HCoC2–DCoO2. *J. Chem. Phys*, *50*, 1920-1927.
25. Ullman, A. M.; Liu, Y.; Huynh, M.; Bediako, D. K.; Wang, H.; Anderson, B. L.; Powers, D. C.; Breen, J. J.; Abruña, H. D.; Nocera, D. G. (2014) Water Oxidation Catalysis by Co(II) Impurities in $Co(III)_4O_4$ Cubanes. *J. Am. Chem. Soc.*, *136*, 17681-17688.
26. Kwapien, K.; Piccinin, S.; Fabris, S. (2013) Energetics of Water Oxidation Catalyzed by Cobalt Oxide Nanoparticles: Assessing the Accuracy of DFT and DFT+U Approaches against Coupled Cluster Methods. *J. Phys. Chem. Lett.*, *4*, 4223-4230.
27. Bard, A. J.; Faulkner, L. R.; Leddy, J.; Zoski, C. G.: *Electrochemical methods: fundamentals and applications*; wiley New York, 1980; Vol. 2.
28. Reynolds, J. G.; Mauss, B. M.; Daniel, R. C. (2018) The relative viscosity of $NaNO_3$ and $NaNO_2$ aqueous solutions. *J. Mol. Liq.*, *264*, 110-114.